Time evolution of the structure function of quenched Al-Zn and Al-Zn-Mg alloys

S. Komura
Faculty of Integrated Arts and Sciences, Hiroshima University, Hiroshima 730, Japan

K. Osamura
Faculty of Engineering, Kyoto University, Kyoto 606, Japan

H. Fujii and T. Takeda
Faculty of Integrated Arts and Sciences, Hiroshima University, Hiroshima 730, Japan
(Received 23 April 1984; revised manuscript received 26 July 1984)

The decomposition of Al—6.8 at. % Zn and Al—10 at. % Zn binary alloys and ternary alloys with the further addition of 0.1 at. % Mg, quenched into the miscibility gap and aged at different temperatures (18, 40, and 80 °C), has been studied by small-angle neutron scattering. The scattering cross section $d\Sigma(k,t)/d\Omega$ as a function of scattering vector k at different aging times t has been analyzed in terms of time-evolution theory of the structure function $S(k,t)$, proposed by Furukawa, taking into account the scaling properties of $S(k,t)$, the mobility $M(t)$ of the clusters, and the diffusivity $D_T(k,t)$ of a cluster gas. The results show that a simple dynamical scaling law $S(k,t) \propto R(t)^3 \tilde{S}(kR(t))$ with a characteristic cluster size $R(t) \propto t^a$ and a universal scaling function $\tilde{S}(x) \propto x^2/(\gamma/2+x^{2+\gamma})$ holds for a wide range of aging times for various samples with different aging temperatures. From the analysis we could extract the time evolution of $M(t)$ and $D_T(k,t)$, which should determine the evolution of $S(k,t)$, and thus we were able to calculate numerically the time evolution of $d\Sigma(k,t)/d\Omega$ in good agreement with corresponding observed quantities.

I. INTRODUCTION

The process of decomposition in binary systems such as alloys, glasses, and liquid mixtures, following quenching from the homogeneous state into the miscibility gap, has been studied for a long time not only because of its practical importance in metallurgy and the development of materials, but also from the point of view of nonequilibrium statistical physics. The early stages of the decomposition process can be interpreted in terms of either the nucleation and growth mechanism of Becker and Döring[1] or the spinodal decomposition mechanism by Cahn and Hilliard,[2] Hillert,[3] and Cook.[4] The former mechanism was refined into the microscopic cluster theory of nucleation developed by Binder and Stauffer.[5] The spinodal decomposition mechanism was successfully developed into a nonlinear theory by Langer, Bar-on, and Miller.[6]

The later stages of the decomposition process were studied by Lifshitz and Slyozov[7] for alloys and by Siggia[8] for liquids. In the later stages of the decomposition, clusters aggregate by a diffusion mechanism and coalesce into larger clusters accompanied by a decrease in the free energy of the system due to the smaller surface energy. The repetition of this process increases the cluster size $R(t)$ in a rather simple manner according to the power law

$$R(t) \propto t^a . \tag{1}$$

Correspondingly, the diffusivity of the cluster $D(t)$ decreases as

$$D(t) \propto R(t)^{-(d+1)} \propto t^{-a(d+1)} . \tag{2}$$

This fact was first noticed by Binder and Stauffer.[9] This idea was developed into a scaling formalism by Furukawa;[10] he proposed that the structure function $S(k,t)$ of the system at the time t can be scaled with a single length parameter $R(t)$ such that

$$S(k,t) \propto R(t)^d \tilde{S}(kR(t)) , \tag{3}$$

where $\tilde{S}(x)$ is a universal scaling function and d is the dimensionality of the system.

Subsequently, the scaling relation was found to hold in the results of a computer simulation using a kinetic Ising model by Marro, Lebowitz, and Kalos.[11] The relation was further confirmed in real systems, for example, in liquid mixtures by Chou and Goldburg[12] and in binary alloys by Hennion, Ronzaud, and Guyot.[13]

A universal scaling function $\tilde{S}(x)$ was proposed by Rikvold and Gunton[14] who assumed a model of spherical clusters surrounded by depletion zones (cluster regime). Furukawa[15] has obtained a scaling function of the form

$$\tilde{S}(x) \propto \frac{x^2}{\gamma/2+x^{2+\gamma}} , \tag{4}$$

where $x = kR(t)$ and $\gamma = d+1$ for off-critical concentrations (cluster regime) and $\gamma = 2d$ for the critical concentration (percolation regime) in the dynamic scaling theory. This theory takes into account the scaling of the mobility $M(t)$ and susceptibility $\chi(k,t)$ of the clusters such that

$$M(t) \propto R(t)^{-\zeta} \tag{5}$$

and

$$\chi(k,t) \propto R(t)^d \tilde{\chi}(kR(t)) , \tag{6}$$

where ζ is an exponent related to the exponent a in (1) and

$\tilde{\chi}(x)$ is a scaling function.

In this paper we observed the small-angle neutron scattering cross section $d\Sigma(k,t)/d\Omega$ from quenched Al-Zn and Al-Zn-Mg alloys, and compared it with a theoretical calculation of the structure function $S(k,t)$ in the framework of Furukawa's theory.[10,15] The results show that the scattering cross section can be scaled by the length parameter $R(t)$ in terms of the scaling function $\tilde{S}(x)$, as given by (4). Good agreement was obtained not only for the scaling function $\tilde{S}(x)$, but also for the time evolution of $S(k,t)$ including the absolute values of k, t, and $S(k,t)$, if we take reasonable values of the mobility $M(t)$ and the susceptibility $\chi(k,t)$. Conversely, we could determine the values of the mobility and the susceptibility that account for the time evolution of $S(k,t)$.

We used the ternary alloys with the addition of 0.1 at. % of the third element Mg to the corresponding binary Al-Zn system in order to stabilize the quenched-in vacancies, and accordingly to control the diffusion process of atoms governed by such vacancies. In fact, the ternary alloys show simpler behavior with respect to the decomposition process than the corresponding binary system, in which quenched-in vacancies vanish rapidly and show a kind of saturation in the decomposition process. In this sense the ternary system represents a more ideal case of the decomposition of the pseudobinary system.

In Sec. II the theoretical background for the present study of decomposition is given, including the definitions and properties of the structure function, the neutron scattering cross section, and the two-phase model of the binary system. In Sec. III the small-angle neutron scattering experiment and the sample preparation are described. The results of the small-angle neutron scattering are given in Sec. IV. In Sec. V the general trends, the scaling properties, and the time evolution of the scattering cross section are discussed. The conclusions are summarized in Sec. VI.

II. THEORY

A. Definition of the structure function

The structure function $S(\vec{k},t)$ is the Fourier transform of the space-correlation function $G(\vec{r},t)$ of the composition $\eta(\vec{r},t)$ at time t as a parameter. These functions are given by

$$S(\vec{k},t)=\int G(\vec{r},t)e^{i\vec{k}\cdot\vec{r}}d\vec{r} \tag{7}$$

and

$$G(\vec{r},t)=\frac{1}{V}\int[\eta(\vec{r}',t)-\bar{\eta}][\eta(\vec{r}+\vec{r}',t)-\bar{\eta}]d\vec{r}' , \tag{8}$$

$$\eta(\vec{r},t)=\frac{1}{\bar{n}_A+\bar{n}_B}[n_A(\vec{r},t)-n_B(\vec{r},t)] , \tag{9}$$

where $n_A(\vec{r},t)$ and $n_B(\vec{r},t)$ are densities of A and B atoms, respectively, and $\bar{n}_A$ and $\bar{n}_B$ are respective average densities ($-1\le\eta\le1$) and

$$\bar{\eta}=\frac{\bar{n}_A-\bar{n}_B}{\bar{n}_A+\bar{n}_B}=1-2c , \tag{10}$$

where

$$c=\bar{n}_B/(\bar{n}_A+\bar{n}_B) \tag{11}$$

is the B atom concentration and V is the volume of the system ($0\le c\le1$).

The space-correlation function $G(\vec{r},t)$ of the composition $\eta(r,t)$ can be expressed by the space cross-correlation function $g_{AB}(\vec{r},t)$ of the densities $n_A(\vec{r},t)$ and $n_B(\vec{r},t)$,

$$G(\vec{r},t)=1-\frac{1}{(\bar{n}_A+\bar{n}_B)^2}[(\bar{n}_A-\bar{n}_B)^2+4g_{AB}(\vec{r},t)] , \tag{12}$$

where

$$g_{AB}(\vec{r},t)=\frac{1}{V}\int n_A(\vec{r}',t)n_B(\vec{r}+\vec{r}',t)d\vec{r}' . \tag{13}$$

The function $g_{AB}(\vec{r},t)$ is more tractable than $G(\vec{r},t)$ in a realistic model of a binary system.

If we integrate $S(\vec{k},t)$ over all $\vec{k}/(2\pi)^3$, we obtain

$$S(\text{calc})=\frac{1}{(2\pi)^3}\int S(\vec{k},t)d\vec{k}=\frac{1}{V}\int[\eta(\vec{r},t)-\bar{\eta}]^2d\vec{r}$$
$$=\langle\eta^2\rangle-\langle\eta\rangle^2 , \tag{14}$$

where $\langle\cdots\rangle$ denotes space averaging $(1/V)\int\cdots dr$. The sum rule (14) shows that $S(\text{calc})$ is equal to the mean-square deviation of the local composition from the average composition. If we assume further that $S(\vec{k},t)$ is isotropic in the space of $\vec{k}$, we obtain

$$S(\text{calc})=\frac{4\pi}{(2\pi)^3}\int_0^\infty k^2S(k,t)dk , \tag{15}$$

which is easier to calculate than (14).

B. Time evolution of the structure function

Furukawa[10] has derived an equation for the time evolution of the structure function of the form

$$\frac{d}{dt}S(k,t)=2M(t)k_BTk^2[1-\chi^{-1}(k,t)S(k,t)] , \tag{16}$$

where $M(t)$ is the mobility of the clusters and depends on the time according to the scaling law

$$M(t)=M_0[R(t)]^{-\zeta}=M(1)t^{-a\zeta} , \tag{17}$$

where $R(t)$ is a measure of the cluster size and grows with time according to a power law

$$R(t)=R(1)t^a . \tag{18}$$

Furukawa found a relation between the exponents ζ and a

$$a=(d+\zeta+2)^{-1} . \tag{19}$$

Assuming a scaling property for $\chi(k,t)$ of the form

$$\chi^{-1}(k,t)=\alpha^{-1}[R(t)]^{-d}\tilde{\chi}^{-1}(kR(t)) , \tag{20}$$

he obtained a scaling property for the solution $S(k,t)$ of (16) of the form

$$S(k,t)=\alpha[R(t)]^d\tilde{S}(kR(t)) . \tag{21}$$

Here the constant α is

$$\alpha=\frac{2}{(1-a\zeta)(2/\gamma+1)} \tag{22}$$

and the universal scaling functions $\tilde{\chi}^{-1}(x)$ and $\tilde{S}(x)$ have the forms

$$\tilde{\chi}^{-1}(x)=\frac{x^{\gamma}}{1+\gamma/2}\frac{\gamma(d+\gamma+4)/(2d+4)+x^{2+\gamma}}{\gamma/2+x^{2+\gamma}} \tag{23}$$

and

$$\tilde{S}(x)=\frac{(1+\gamma/2)x^2}{\gamma/2+x^{2+\gamma}} . \tag{24}$$

The scaling function $\tilde{S}(x)$ was originally derived[15] from the asymptotic forms

$$\tilde{S}(x)\propto\begin{cases}x^2 & \text{for small } x\\ x^{-\gamma} & \text{for large } x ,\end{cases} \tag{25}$$

and the normalization property $\tilde{S}(1)=1$. These asymptotic forms are reasonable assumptions, since at small x the time-evolution equation (16) has an asymptotic form

$$\frac{d}{dt}S(k,t)\simeq 2M(t)k_BTk^2 \tag{26}$$

due to the conservation of the number of A and B atoms (conservation of the order parameter), and at large x the cross-correlation function (13) should have the form

$$g_{AB}(r,t)\propto\frac{[R(t)]^{d-1}r}{[R(t)]^d}=r[R(t)]^{-1} , \tag{27}$$

and thus

$$S(k,t)\propto k^{-(d+1)}[R(t)]^{-1} \tag{28}$$

in the case of off-critical concentrations. This latter asymptotic form is identical with Porod's law, which is well known in small-angle x-ray scattering.[16] The scaling function $\tilde{\chi}(x)$ in (23) was derived[15] from the time-evolution equation (16) assuming the scaling function (24) together with the initial condition $\tilde{S}(0)\tilde{\chi}^{-1}(0)=0$.

C. Numerical calculation of the structure function

It is interesting to note that if we calculate the integral of $S(k,t)$ according to (15) with substitution of (21) and (24), we obtain

$$S(\text{calc})=\frac{4\pi\alpha\beta}{(2\pi)^3}=\frac{\alpha\beta}{2\pi^2} , \tag{29}$$

where

$$\beta=\int_0^{\infty}x^2\tilde{S}(x)dx . \tag{30}$$

For off-critical concentrations $\gamma=d+1$, and for the three-dimensional case $d=3$, we have

$$\tilde{S}(x)=\frac{3x^2}{2+x^6} \tag{31}$$

and $\beta=2.800$ by numerical calculation. In the same case α in (22) is simplified and gives

$$\alpha=\frac{4}{3(1-a\zeta)} , \tag{32}$$

and (23) gives

$$\tilde{\chi}^{-1}(x)=\frac{x^4(44/10+x^6)}{3(2+x^6)} . \tag{33}$$

The calculated structure function can be normalized by dividing $S(k,t)$ by $S(\text{calc})$ to give

$$\mathcal{S}^{\text{calc}}(k,t)=\frac{1}{S(\text{calc})}S(k,t) , \tag{34}$$

which should be compared with the normalized cross section $\mathcal{S}^{\text{obs}}(k,t)$ in (48) obtained from the experiment.

It should be noted that constants $M(1)$ in (17) and $R(1)$ in (18) cannot be chosen independently. There is a relation[17] between $M(1)$ and $R(1)$,

$$M(1)=M_0[R(1)]^{-\zeta}=\frac{1}{2k_BT}a(d+2)\left[\frac{2}{\gamma}+1\right][R(1)]^{d+2} , \tag{35}$$

which should be obeyed if $S(k,t)$ has the scaling property in (21).

The diffusion coefficient is then given by

$$\begin{aligned}D_T(k,t)&=k_BTM(t)\chi^{-1}(k,t)\\&=k_BTM_0[R(t)]^{-\zeta}\chi^{-1}(k,t)\\&=k_BTM(1)t^{-a\zeta}\chi^{-1}(k,t)\end{aligned} \tag{36}$$

for given k and t at the temperature T.

D. Neutron scattering cross section

What we observe from the neutron scattering experiment is the macroscopic cross section $d\Sigma/d\Omega$ in units of $\text{cm}^{-1}\,\text{sr}^{-1}$, which is defined as the scattering cross section per unit volume of the sample per unit solid angle. The macroscopic cross section is given by

$$\frac{d\Sigma}{d\Omega}=\int G'(\vec{r})e^{i\vec{k}\cdot\vec{r}}d\vec{r} , \tag{37}$$

where

$$G'(r)=\frac{1}{V}\int[\rho(\vec{r}')-\bar{\rho}][\rho(\vec{r}+\vec{r}')-\bar{\rho}]d\vec{r}' \tag{38}$$

is the space-correlation function of the scattering amplitude density $\rho(\vec{r})$, which is defined for a small volume v around the position $\vec{r}$ as

$$\rho(\vec{r})=\int_v b_i\delta(\vec{r}_i-\vec{r})d\vec{r}\Big/\int_v d\vec{r}=\frac{1}{v}\sum_i b_i , \tag{39}$$

where b_i is the scattering amplitude of the atom at the site $\vec{r}_i$ and the sum extends over the small volume v around $\vec{r}$. $\bar{\rho}$ is the average of $\rho(\vec{r})$ over the total volume V. The formulas (37) and (38) correspond to (7) and (8), respectively, in the structure-function formalism.

If we integrate $d\Sigma(\vec{k})/d\Omega$ over all $\vec{k}/(2\pi)^3$, we obtain

$$\begin{aligned}\Sigma(\text{calc})&=\frac{1}{(2\pi)^3}\int\frac{d\Sigma(\vec{k})}{d\Omega}d\vec{k}=\frac{1}{V}\int[\rho(\vec{r})-\bar{\rho}]^2d\vec{r}\\&=\langle\rho^2\rangle-\langle\rho\rangle^2 ,\end{aligned} \tag{40}$$

which is similar to (14) for the structure function. Such integrals can be calculated from the experiment for the isotropic case by

$$\Sigma(\text{obs})=\frac{4\pi}{(2\pi)^3}\int_0^\infty k^2\frac{d\Sigma(k)}{d\Omega}dk\ . \tag{41}$$

In practice the integration must be replaced by a sum for a finite range of the measured values of k with finite Δk instead of dk. The isotropic assumption is justified by the experiment of Hennion, Ronzaud, and Guyot.[13]

E. Two-phase model for the cross section

The integral cross section $\Sigma(\text{calc})$ in (40) can be calculated from the two-phase model in which the average B concentration is c and the total system is split into cluster particles with c_p B concentration, and the surrounding matrix with c_m B concentration (Fig. 1).

Taking the volume of an atom to be v_a, the average, particle, and matrix scattering amplitude densities $\bar{\rho}$, ρ_p, and ρ_m, respectively, are

$$\begin{aligned}\bar{\rho}&=\frac{1}{v_a}[(1-c)b_A+cb_B]\ ,\\ \rho_p&=\frac{1}{v_a}[(1-c_p)b_A+c_pb_B]\ ,\\ \rho_m&=\frac{1}{v_a}[(1-c_m)b_A+c_mb_B]\ ,\end{aligned} \tag{42}$$

where b_A and b_B are scattering amplitudes of A and B atoms, respectively.

Since the volume fraction of particles f_p and that of the matrix f_m are given by the lever rule, respectively, as

$$\begin{aligned}f_p&=\frac{c-c_m}{c_p-c_m}=1-f_m\ ,\\ f_m&=\frac{c_p-c}{c_p-c_m}=1-f_p\ ,\end{aligned} \tag{43}$$

and the average of ρ and ρ^2 are given by

$$\begin{aligned}\langle\rho\rangle&=f_p\rho_p+(1-f_p)\rho_m\ ,\\ \langle\rho^2\rangle&=f_p\rho_p^2+(1-f_p)\rho_m^2\ ,\end{aligned} \tag{44}$$

the integral (40) can be calculated as

$$\Sigma(\text{calc})=f_p(1-f_p)(\rho_p-\rho_m)^2\ . \tag{45}$$

By the use of (42) we obtain

$$\rho_p-\rho_m=\frac{1}{v_a}(c_m-c_p)(b_A-b_B)\ , \tag{46}$$

and therefore

$$\begin{aligned}\Sigma(\text{calc})&=\frac{1}{v_a^2}f_p(1-f_p)(c_m-c_p)^2(b_A-b_B)^2\\ &=\frac{1}{v_a^2}(c-c_m)(c_p-c)(b_A-b_B)^2\ .\end{aligned} \tag{47}$$

The scattering cross section $d\Sigma(k,t)/d\Omega$ may be divided by $\Sigma(\text{calc})$ to obtain the normalized experimental structure function

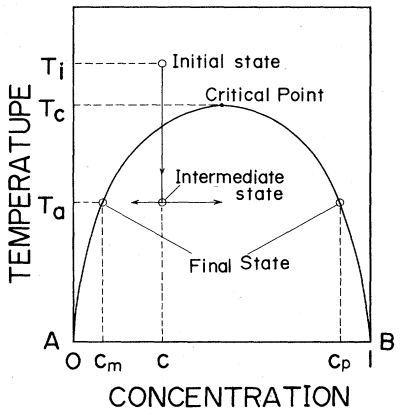

FIG. 1. Schematic phase diagram of binary A-B system. Starting from the initial state at temperature T_i with average B atom concentration c, the system reaches the final state at temperature T_a with particle concentration c_p and matrix concentration c_m.

$$\mathcal{S}^{\text{obs}}(k,t)=\frac{1}{\Sigma(\text{calc})}\frac{d\Sigma(k,t)}{d\Omega}\ , \tag{48}$$

which should be compared with $\mathcal{S}^{\text{calc}}(k,t)$ in (34).

III. EXPERIMENT

A. Small-angle neutron scattering experiment

The small-angle neutron scattering experiment was performed at the Kyoto University Reactor (5 MW) with a neutron guide tube and a 6-m-long small-angle scattering apparatus. The description of the apparatus is given in detail in separate papers[18] and therefore is not repeated here. The wavelength used was about 4 Å, which was produced by a mechanical velocity selector. The area of incidence of the neutrons on the sample was 6×28 mm^2 and the thickness of the sample was 10 mm. The scattered neutrons were detected by a one-dimensional position-sensitive detector. The absolute value of the scattering cross section was calibrated against a standard vanadium sample.

The observed cross sections were corrected for the background. However, no corrections were made for the finite resolution of the scattering vector k of the spectrometer, since the scattering curves were fairly broad. Corrections for multiple Bragg scattering were unnecessary, since we used fairly long wavelength neutrons of 4 Å. The Placzek correction for multiple phonon scattering was found to be negligible, since the experiment was performed at 77 K.

B. Sample preparation

Two binary alloys, Al—6.8 at.% Zn (sample B) and Al—10 at.% Zn (sample D), and two ternary alloys (samples A and C), with the further addition of 0.1 at.% Mg to the corresponding binary alloys, were made from the melt. They were shaped into rectangular parallelepipeds with dimensions of $10\times10\times32$ mm^3. They were homogenized at 300 °C, quenched in brine at −20 °C, and subsequently kept at 77 K.

TABLE I. Composition, aging temperature, exponent a' in (52), and comparison of the observed and calculated integral cross section $\Sigma'(\text{obs})$, $\Sigma(\text{obs})$, and $\Sigma(\text{calc})$, defined in (50), (58), and (47), respectively.

Sample	Composition Al + Zn (at. %)	Mg (at. %)	Aging temp. (°C)	a'	$\Sigma'(\text{obs})$ (10^{-14} Å^{-4})	$\Sigma(\text{obs})$ (10^{-14} Å^{-4})	$\Sigma(\text{calc})$ (10^{-14} Å^{-4})	$\frac{\Sigma'(\text{obs})}{\Sigma(\text{calc})}$	$\frac{\Sigma(\text{obs})}{\Sigma(\text{calc})}$
A	6.8	0.1	80	0.16	3.1	3.8	4.4	0.70	0.86
B	6.8		80	0.11	2.2	3.0	4.4	0.50	0.68
C	10	0.1	80	0.18	4.1	6.0	7.7	0.53	0.78
D	10		80	0.34	4.0	5.8	7.7	0.52	0.75
A'	6.8	0.1	40	0.11	10.3	16	9.2	1.12	1.74
B'	6.8		40	0.22	10.0	25	9.2	1.10	2.72
C'	10	0.1	18	0.06	5.6	8.0	10.1	0.56	0.79
D'	10		18	0.17	6.4	8.8	10.1	0.63	0.87

Eight different samples were prepared in all: they were ternary and binary alloys with 6.8 at. % Zn aged at 80 °C (samples *A*, *B*) and 40 °C (*A'*, *B'*), respectively, and those with 10 at. % Zn aged at 80 °C (*C*, *D*) and 18 °C (*C'*, *D'*), respectively, which are listed in Table I and shown in Fig. 2. Note that the samples *C'* and *D'* lie inside the supposed spinodal line in the phase diagram. They were aged for various periods ranging from 1, 2, 5, 10, 20, 50, 100, 200, 500, 1000 (or 800) min before the measurements. Each measurement was carried out at 77 K to suppress the aging and typically took half an hour.

IV. RESULTS

Some of the present results on the samples *A'* and *B'* have already been published[19] and this study has been extended to six other samples (*A*, *B*, *C*, *D*, *C'*, *D'*) in another independent experiment. A summary of the present study has been reported in the Rapid Communications of this journal.[20]

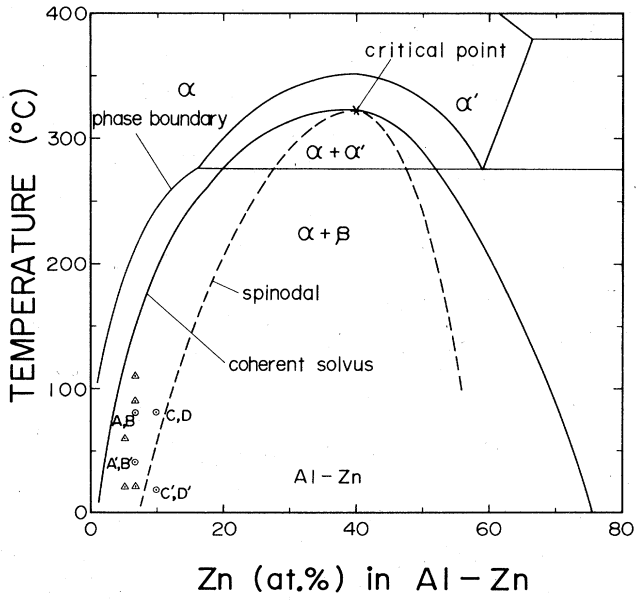

FIG. 2. Phase diagram of Al-Zn system. Circles represent the concentrations and aging temperatures of our samples (ternary alloys *A*, *A'*, *C*, *C'* and binary alloys *B*, *B'*, *D*, *D'*) in this paper. Triangles represent those of Hennion *et al.* (Ref. 13).

Figure 3 shows the neutron scattering cross section $d\Sigma(k,t)/d\Omega$ as a function of scattering vector k at various aging periods t for different compositions and different aging temperatures of the eight samples (*A*, *B*, *C*, *D*, *A'*, *B'*, *C'*, *D'*), respectively. Note that all the abscissas for k have the same scale, while some of the ordinates for $d\Sigma/d\Omega$ have different scales from others. On the whole there is a trend that as the aging time t increases the maximum of the curve shifts towards smaller k and the maximum value increases.

Figure 4 shows the same cross section $d\Sigma(k,t)/d\Omega$ as in Fig. 3 as a function of aging period t at various scattering vectors k for the eight samples. The binary samples without 0.1 at. % Mg (*B*, *B'*, *D*, *D'*) show the trend that the growth of clusters ceases at an intermediate time and reaches saturation. In the ternary samples (*A*, *A'*, *C*, *C'*) the growth of clusters continues at this range of aging time, although the growth rate is smaller than the binary alloys.

Our neutron scattering cross sections are in agreement with those measured by Hennion, Ronzaud, and Guyot[13] from single-crystal binary alloys Al-Zn with similar concentrations aged at different temperatures (Fig. 2), except that our polycrystalline samples reached saturation at earlier aging times t than in the single-crystal case.

V. DISCUSSION

A. Character of the scattering cross section

It is possible to analyze the neutron scattering data from the point of view of the two-phase model and to extract the size of the clusters, the distance between clusters, and the cluster density. Since such analysis will be given later in Sec. V E, we will focus first only on the analysis of the structure function.

From each of the scattering curves $d\Sigma(k,t)/d\Omega$ as a function of k in Fig. 3, we can calculate the first and second moment, $k_1(t)$ and $k_2(t)$, respectively, at each ag-

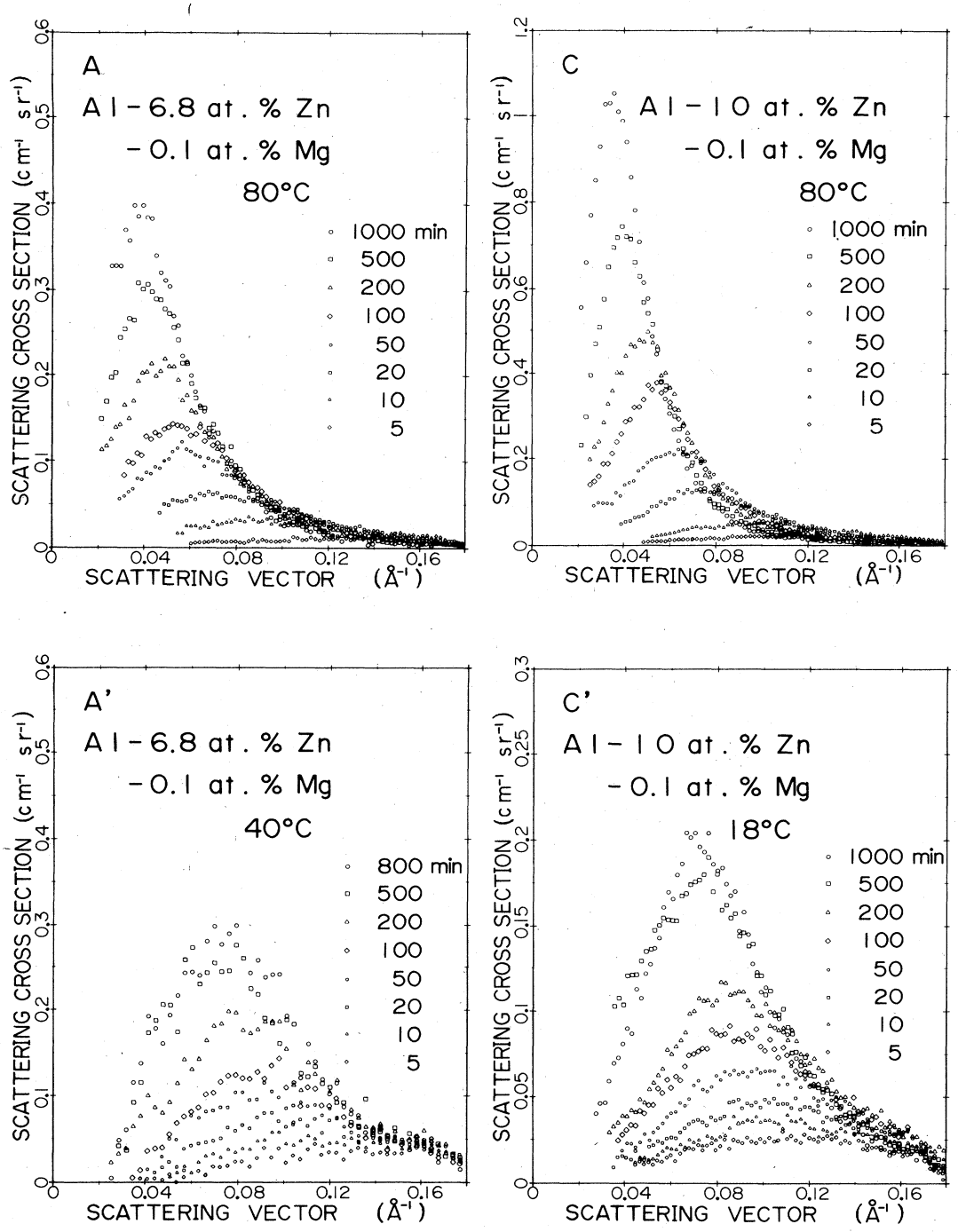

FIG. 3. Neutron scattering cross section $d\Sigma/d\Omega$ ($\mathrm{cm}^{-1}\,\mathrm{sr}^{-1}$) as a function of scattering vector k ($\mathrm{\AA}^{-1}$) at different aging times t (min) for the eight samples A, B, C, D, A', B', C', D', respectively. Note that the scales of the ordinates are different from each other.

ing time for each sample defined by

$$k_n(t)=\frac{\sum_{k=k_{\min}}^{k_{\max}} k^n \frac{d\Sigma(k,t)}{d\Omega}}{\sum_{k=k_{\min}}^{k_{\max}} \frac{d\Sigma(k,t)}{d\Omega}} \quad (n=1,2)\,, \tag{49}$$

where the sum extends over the measured range of k, i.e., roughly from $k_{\min}=0.02$ to $k_{\max}=0.20$ $\mathrm{\AA}^{-1}$. Instead of using Eq. (41) we can also calculate the following sum:

$$\Sigma'(\mathrm{obs},t)=\frac{4\pi}{(2\pi)^3}\sum_{k=k_{\min}}^{k_{\max}} k^2\frac{d\Sigma(k,t)}{d\Omega}\Delta k\,, \tag{50}$$

where the prime denotes that the sum covers the finite

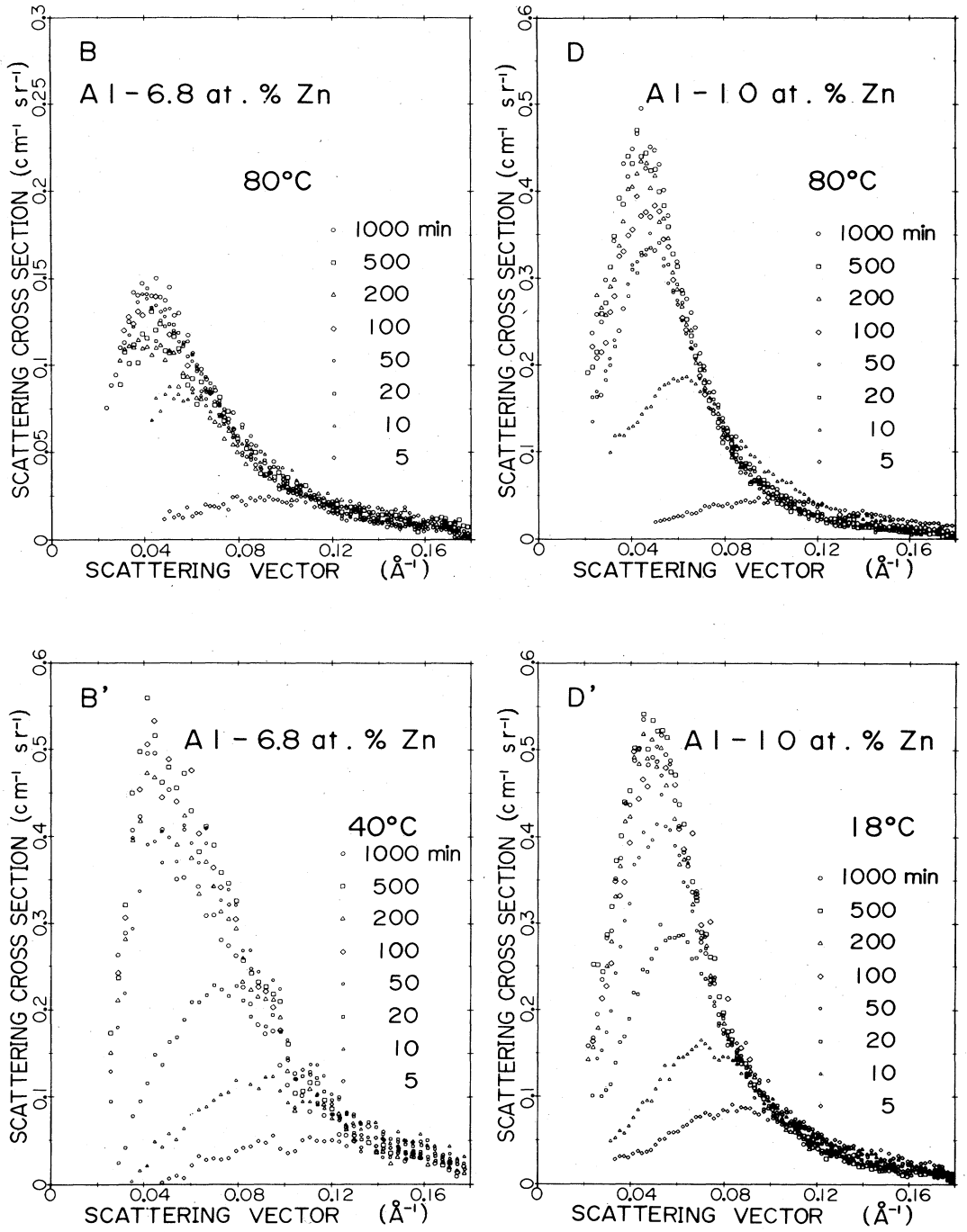

FIG. 3. (*Continued*).

measured range from $k_{\min}$ to $k_{\max}$.

The values of $k_1(t)$, $[k_2(t)]^{1/2}$, the ratio $[k_2(t)]^{1/2}/k_1(t)$, and $\Sigma'(\text{obs},t)$ were plotted logarithmically as a function of aging time t for each sample, although the plots are not shown here. On the whole the ratio $[k_2(t)]^{1/2}/k_1(t)$ was almost constant and independent of aging time, and the value of this ratio ranged between

$$1.0 < [k_2(t)]^{1/2}/k_1(t) < 1.1 \ . \tag{51}$$

Thus we were able to extract the exponent a' in the power law

$$k_1(t) \propto [k_2(t)]^{1/2} \propto t^{-a'} \tag{52}$$

for the overall aging time for the ternary alloys (A, A', C, C') and for a rather limited time range up to 50 min for the binary alloys (B, B', D, D'). The integral cross section $\Sigma'(\text{obs},t)$ has a gradual increase with time t, but becomes almost constant at longer times. The values of a'

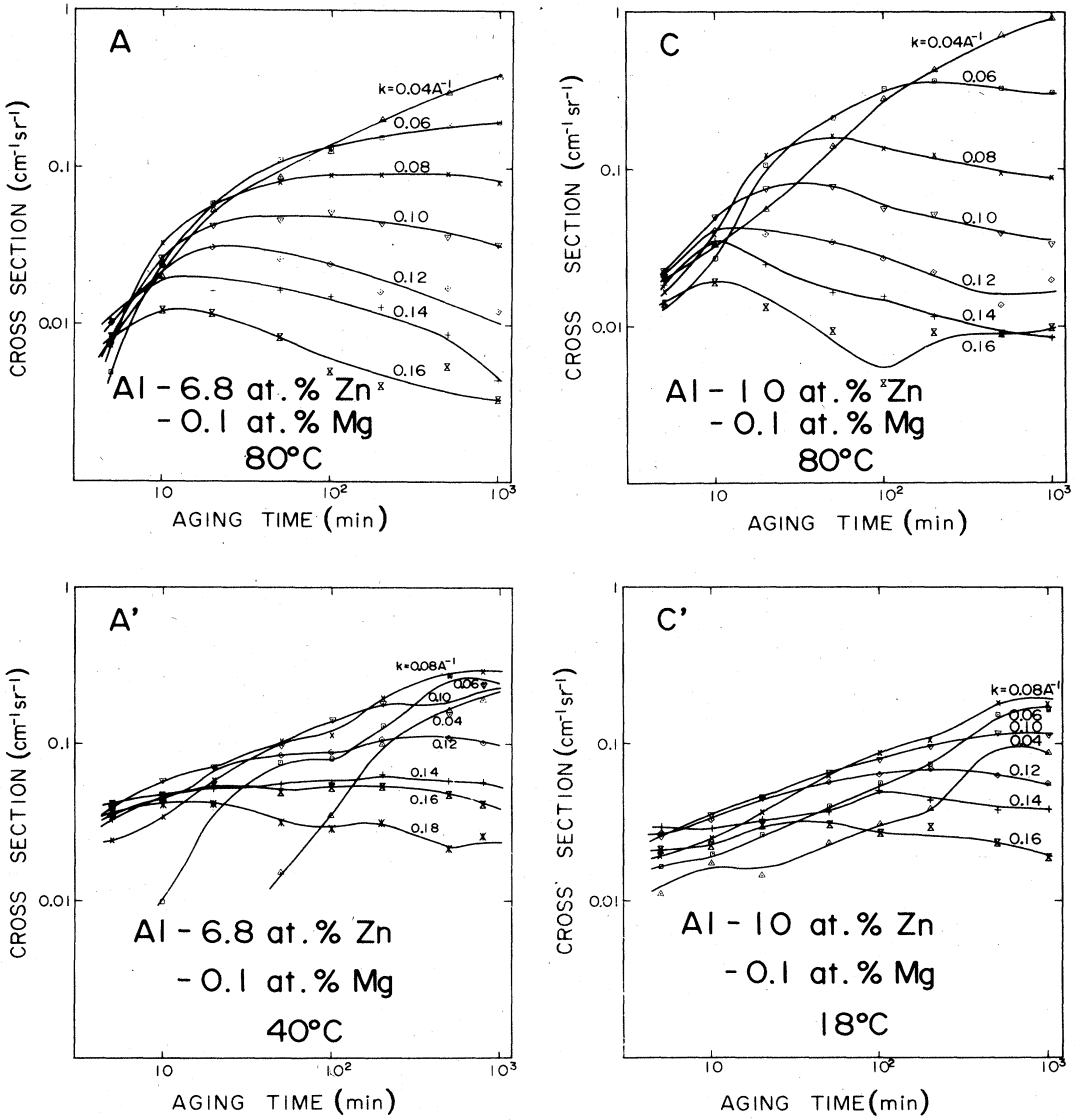

FIG. 4. Same neutron scattering cross section $d\Sigma/d\Omega$ ($\mathrm{cm}^{-1}\mathrm{sr}^{-1}$) as in Fig. 3 as a function of aging time t (min) at different scattering vectors k ($\mathrm{\AA}^{-1}$) for the eight samples.

and the final integral cross section $\Sigma'(\mathrm{obs})$ at $t=1000$ min are listed in Table I.

The values $a'=0.11$ for sample B (80 °C) and $a'=0.22$ for sample B' (40 °C) of the present results are consistent with the values $a'=0.10$ (110 °C), 0.11 (90 °C), and 0.23 (20 °C) for the same binary alloy Al–6.8 at.% Zn observed by Hennion, Ronzaud, and Guyot.[13]

In order to see the asymptotic behavior of $d\Sigma(k,t)/d\Omega$ as a function of k in the limit of either small k or large k, we have shown the same data as in Fig. 3 on log-log plots in Fig. 5. In these figures two straight lines are found expressing the dependence on k^2 for small k and k^{-4} for large k. It is likely that $d\Sigma/d\Omega$ increases like k^2 for small k and decreases like k^{-4} for large k, although the data are somewhat obscured at small k due to the finite resolution of the measurements.

B. Least-squares fit of the scattering cross section

Here we give a proper normalization of the experimental scattering cross section $d\Sigma(k,t)/d\Omega$ to be scaled and compared directly with the Furukawa's scaling function (31). If $\mathcal{S}^{\mathrm{calc}}(k,t)$ in (34) is equal to $\mathcal{S}^{\mathrm{obs}}(k,t)$ in (48) and if the scaling law (21) holds, the scattering cross section should be expressed by

$$\frac{d\Sigma(k,t)}{d\Omega}=\frac{\Sigma(\mathrm{calc})}{S(\mathrm{calc})}S(k,t)$$

$$=\frac{\Sigma(\mathrm{calc})}{S(\mathrm{calc})}\alpha[R(t)]^d\tilde{S}(kR(t))$$

$$=A(t)\tilde{S}(x)\,, \tag{53}$$

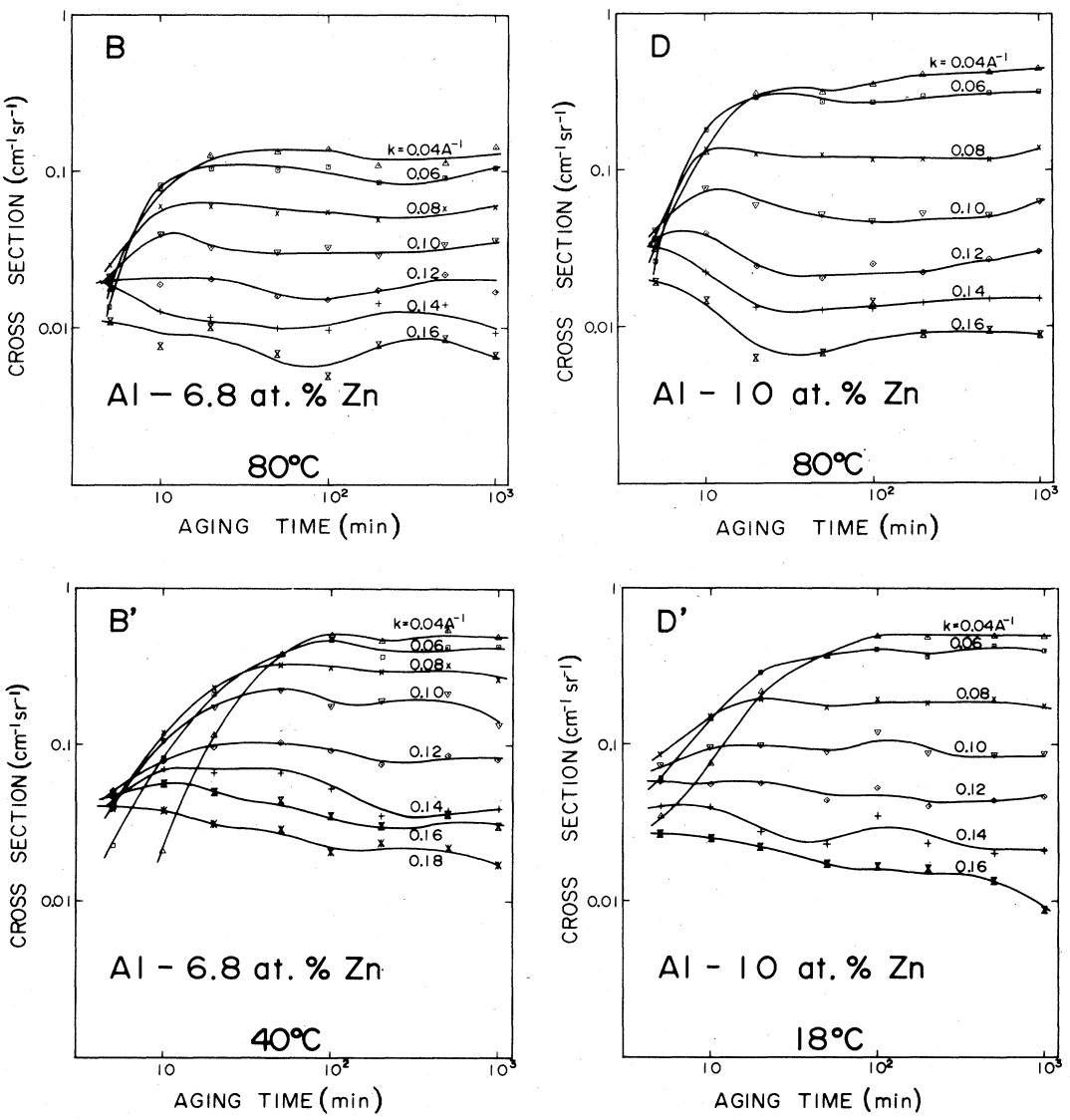

FIG. 4. (*Continued*).

where we have put

$$A(t)=\frac{\Sigma(\text{calc})}{S(\text{calc})}\alpha[R(t)]^d \tag{54}$$

and

$$x=kR(t)=kk_m^{-1}(t) \tag{55}$$

in $\tilde{S}(x)$ defined by (31).

By a least-squares fit of the scattering cross section $d\Sigma(k,t)/d\Omega$ to formula (53), we obtained the two parameters $A(t)$ and $k_m(t)$ for each scattering curve. The values for $A(t)$ and $k_m(t)$ thus obtained are listed in Table II and plotted in Fig 6 for all the data. The scattering cross section $d\Sigma(k,t)/d\Omega$ calculated from (53) with these parameters $A(t)$ and $k_m(t)$ are plotted in Fig. 7 for all the samples as a function of k. The calculated curves are in very good agreement with the original experimental data (Fig. 3). The exponent a governing the exponential growth of $R(t)=k_m^{-1}(t)$ by (18) and a similar exponent b for $A(t)$ given by

$$A(t)=A(1)t^b \tag{56}$$

are determined from Fig. 6 for a certain limited aging time range with corresponding initial values at 1 min of aging time $R(1)$ and $A(1)$. These values are listed in Table III. For most of the data it was difficult to determine a single set of the exponent and the initial value, since each curve has a kink or a curvature. Therefore, in a later calculation we used the values of a for $t>20$ (samples A, C), $t<20$ (B, D), $t<500$ (A', C'), or $t<50$ (B', D') min, which represent the main features of the process of the cluster growth.

We determined $x_{\min}$ and $x_{\max}$ corresponding to the

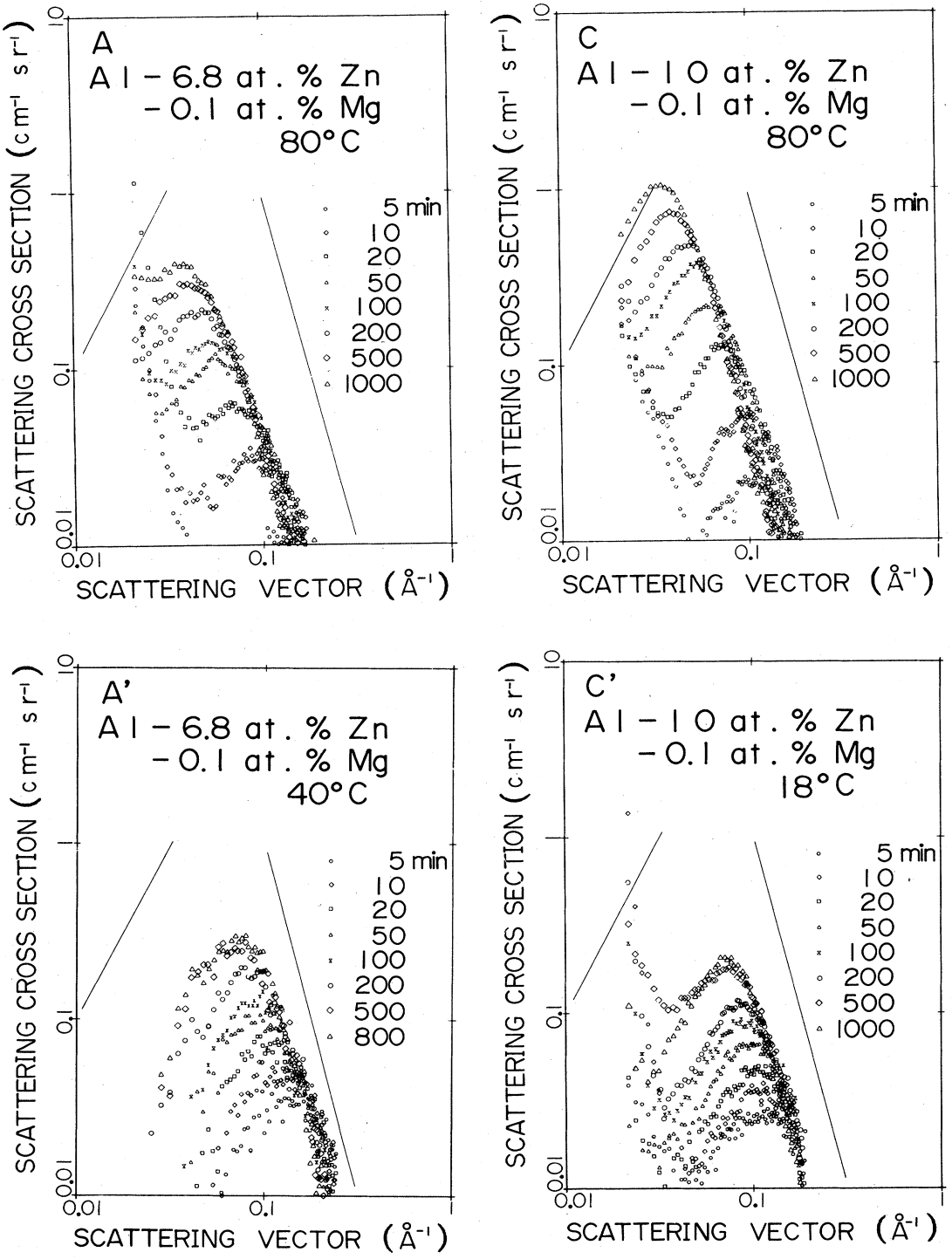

FIG. 5. Logarithmic plot of the scattering cross section $d\Sigma(k,t)/d\Omega$ ($\mathrm{cm}^{-1}\mathrm{sr}^{-1}$) as a function of k (Å^{-1}) at different aging times t (min) for the eight samples. Note that there is a dependence on k^2 for small k and k^{-4} for larger k.

minimum and maximum values $k_{\min}$ and $k_{\max}$, respectively, for each scattering curve by

$$x_{\min}=k_{\min}k_m^{-1}(t) \tag{57a}$$

and

$$x_{\max}=k_{\max}k_m^{-1}(t)\ . \tag{57b}$$

To obtain the integral (41) we calculated the following

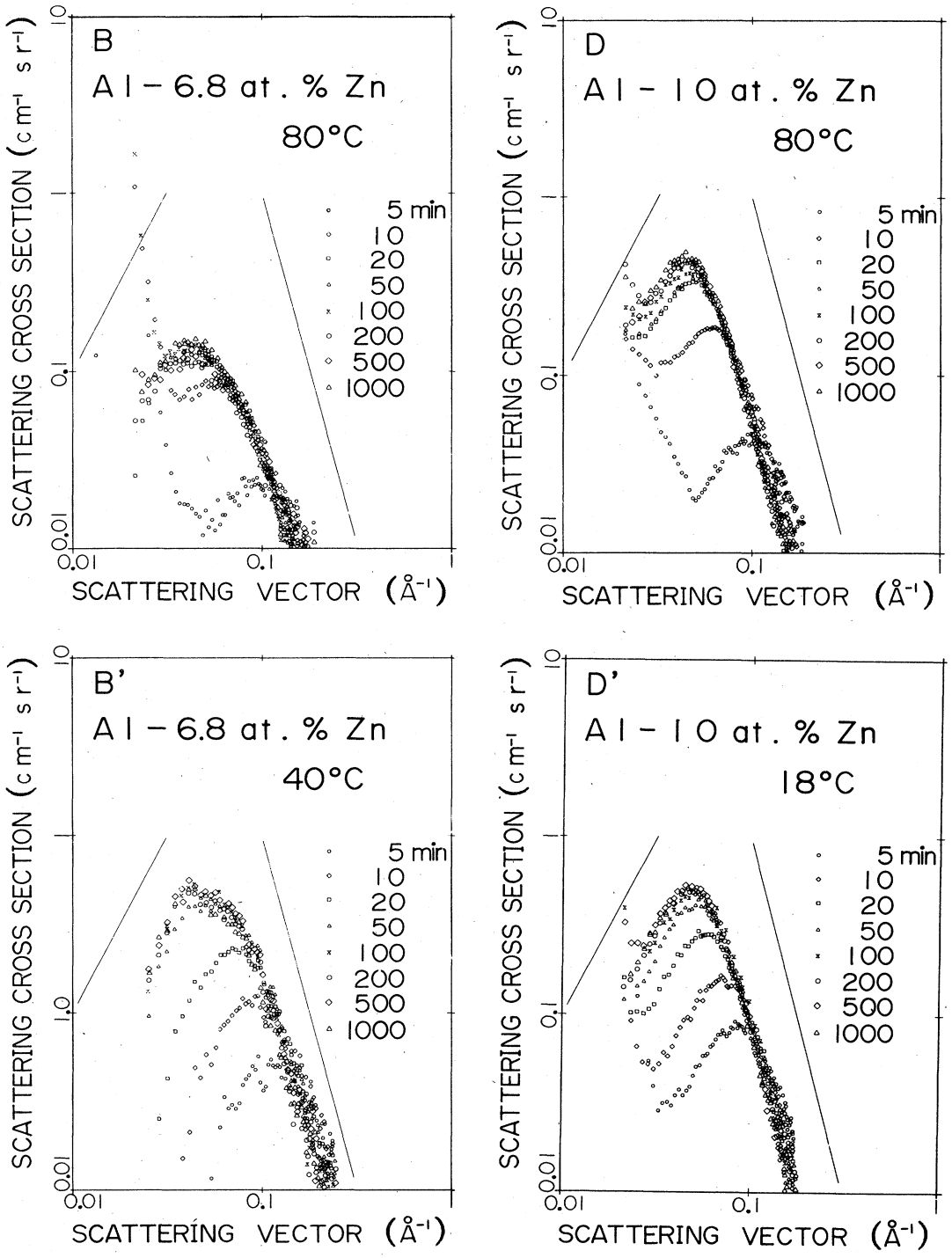

FIG. 5. (*Continued*).

normalized sum:

$$\Sigma(\text{obs},t)=\Sigma'(\text{obs},t)\frac{\int_0^{\infty}x^2\tilde{S}(x)dx}{\int_{x_{\min}}^{x_{\max}}x^2\tilde{S}(x)dx}$$
$$=\frac{4\pi\beta}{(2\pi)^3}\sum_{k=k_{\min}}^{k_{\max}}k^2\frac{d\Sigma(k,t)}{d\Omega}\Delta k\Big/\int_{x_{\min}}^{x_{\max}}x^2\tilde{S}(x)dx\ , \tag{58}$$

which is the sum $\Sigma'(\text{obs},t)$ in (50) multiplied by a factor to remove the effect of the finite-measured range of k. The values for $\Sigma(\text{obs},t)$ are plotted in Fig. 6 for all the samples. The logarithmic (geometric) average of $\Sigma(\text{obs},t)$ for each sample $\Sigma(\text{obs})$ is listed in Table I. Figure 6 shows that the values of $\Sigma(\text{obs},t)$ are nearly constant for a wide range of aging times t.

The values for an integral cross section with finite and

TABLE II. Values of $A(t)$ and $k_m(t)$ defined in (53), (31), and (55) at each aging time t for all the samples; $d\Sigma(k,t)/d\Omega = A(t)3[kk_m^{-1}(t)]^2/\{2+[kk_m^{-1}(t)]^6\}$.

Sample	A ($cm^{-1}sr-1$) k_m (Å^{-1})	Aging time t (min) 5	10	20	50	100	200	500	1000 (*800)
A	$A(t)$	0.011 6	0.033 8	0.066 1	0.119 7	0.152 7	0.228 7	0.323 3	0.415 7
	$k_m(t)$	0.112 39	0.092 02	0.074 16	0.059 92	0.056 15	0.046 82	0.042 73	0.038 76
B	$A(t)$	0.026 5	0.088 8	0.122 7	0.147 8	0.148 0	0.131 1	0.135 0	0.162 3
	$k_m(t)$	0.099 47	0.060 70	0.053 70	0.046 92	0.046 63	0.046 99	0.048 52	0.046 19
C	$A(t)$	0.024 0	0.051 7	0.123 4	0.219 6	0.353 1	0.475 5	0.705 7	1.037 6
	$k_m(t)$	0.109 24	0.097 90	0.072 57	0.060 87	0.051 50	0.046 74	0.039 42	0.034 58
D	$A(t)$	0.046 3	0.192 8	0.342 4	0.340 3	0.393 9	0.430 2	0.455 0	0.473 0
	$k_m(t)$	0.100 10	0.060 74	0.049 02	0.047 96	0.045 68	0.044 84	0.044 45	0.045 00
A'	$A(t)$	0.043 3	0.059 5	0.084 0	0.107 9	0.130 2	0.193 5	0.277 1	*0.295 1
	$k_m(t)$	0.141 43	0.124 13	0.109 61	0.095 87	0.090 59	0.082 90	0.072 48	*0.073 34
B'	$A(t)$	0.060 4	0.120 3	0.233 9	0.457 6	0.541 7	0.496 1	0.566 6	0.500 9
	$k_m(t)$	0.121 98	0.093 83	0.075 12	0.059 35	0.053 31	0.053 11	0.052 54	0.050 40
C'	$A(t)$	0.030 0	0.039 6	0.051 1	0.069 8	0.090 7	0.113 2	0.189 0	0.192 5
	$k_m(t)$	0.110 13	0.106 64	0.101 65	0.096 05	0.089 36	0.086 62	0.071 08	0.071 09
D'	$A(t)$	0.090 8	0.158 4	0.292 3	0.415 6	0.500 1	0.505 5	0.541 6	0.518 0
	$k_m(t)$	0.086 99	0.071 57	0.058 25	0.051 59	0.050 56	0.048 84	0.048 34	0.048 39

TABLE III. Exponents a, ζ, b, and initial characteristic size $R(1)=k_m^{-1}(1)$, peak cross section $A(1)$, and mobility $M(1)$ at $t=1$ min. [$R(t)=R(1)t^a$ from (18), $A(t)=A(1)t^b$ by (56), and $M(t)=M(1)t^{-a\zeta}$ by (17).]

Sample	Time range t (min)	a	$\zeta=\frac{1}{a}-5$	b	$k_m(1)$ (Å^{-1})	$R(1)$ (Å)	$A(1)$ ($cm^{-1}sr^{-1}$)	$k_BTM(1)$ (Å^5/min)
A	<20	0.27		1.57	0.181		0.0010	
	>20	0.15	1.67	0.43	0.108	9.26	0.022	38 283
B	<20	0.59	−3.31	1.72	0.23	4.35	0.0017	3 438
	>20	0		0				
C	<20	0.27		1.11	0.172		0.0034	
	>20	0.18	0.56	0.51	0.116	8.62	0.035	32 138
D	<20	0.72	−3.61	2.07	0.32	3.13	0.0017	805
	>20	0		0				
A'	<500	0.14	2.14	0.53	0.165	6.06	0.0175	4 293
	>500	0		0				
B'	<50	0.38	−2.37	1.00	0.23	4.35	0.0125	2 214
	>50	0		0				
C'	<500	0.08	7.50	0.37	0.130	7.69	0.0165	8 080
	>500	0		0				
D'	<50	0.29	−1.55	1.09	0.142	7.04	0.0150	18 836
	>50	0		0				

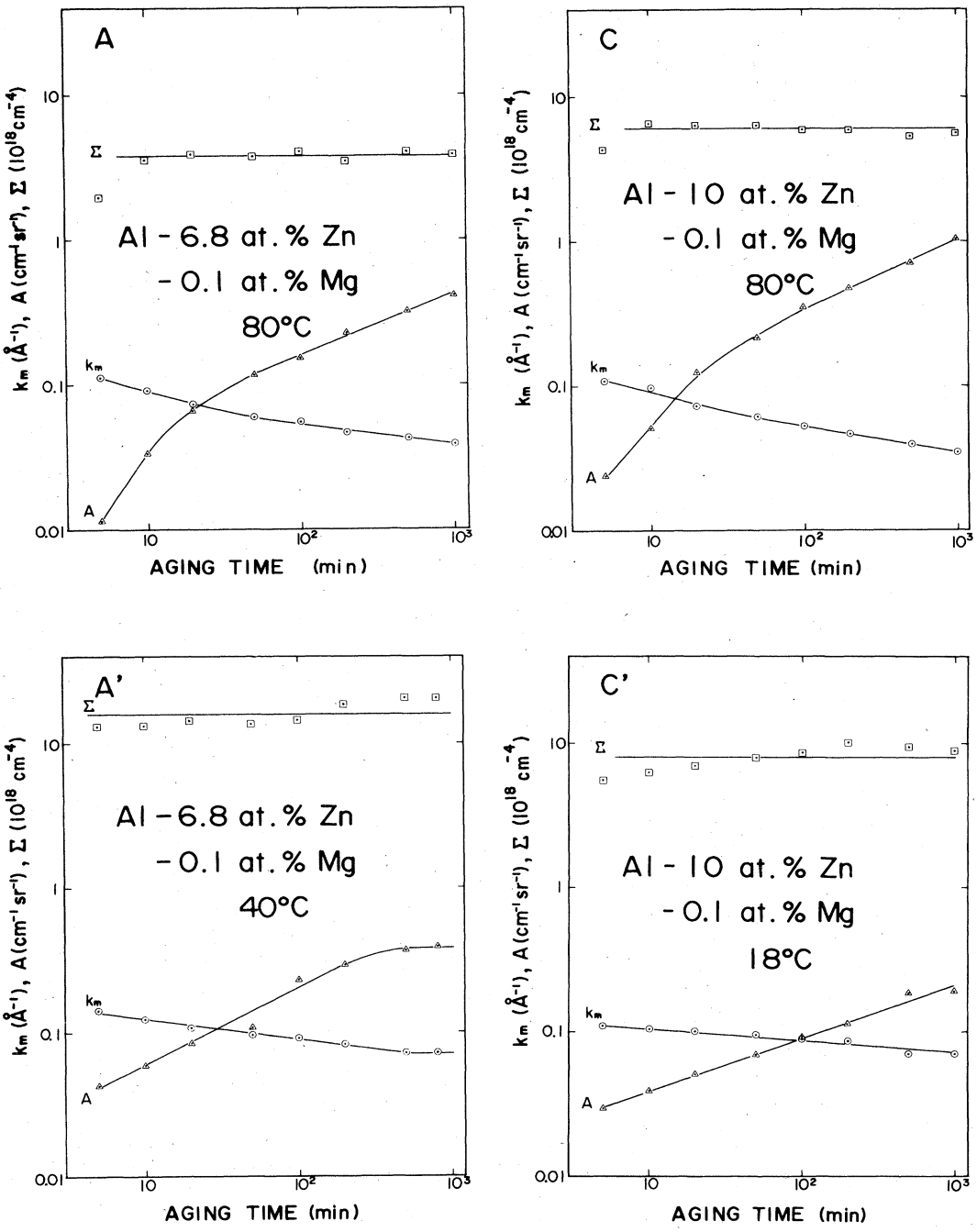

FIG. 6. Aging time dependence of the parameters $k_m(t)$ and $A(t)$, representing the experimental data $d\Sigma(k,t)/d\Omega = A(t)\tilde{S}(x)$ of (53) with $\tilde{S}(x)=3x^2/(2+x^6)$ of (31) and $x=k/k_m(t)$ of (55), and $\Sigma(\text{obs},t)$ as given by (58) for the eight samples.

infinite range of k, $\Sigma'(\text{obs})$ and $\Sigma(\text{obs})$, are compared with those calculated from the two-phase model $\Sigma(\text{calc})$ as given by (47) in Table I, in which the ratios $\Sigma'(\text{obs})/\Sigma(\text{calc})$ and $\Sigma(\text{obs})/\Sigma(\text{calc})$ are shown for each sample. Parameters for the calculation of $\Sigma(\text{calc})$ of (47) are given in Table IV. Although these ratios differ from 1, they are satisfactorily close to 1, if we take into account the crudeness of the two-phase model.

C. Scaled structure function

In the next step we calculated the scaling function $\tilde{S}(x)$ from the observed scattering cross section $d\Sigma(k,t)/d\Omega$. For this purpose we put $\Sigma(\text{obs})$, which is more realistic, in place of $\Sigma(\text{calc})$ in (53) to obtain

$$\frac{d\Sigma(k,t)}{d\Omega}=\frac{\Sigma(\text{obs})}{S(\text{calc})}\alpha k_m^{-3}\tilde{S}(k/k_m(t))\,. \tag{59}$$

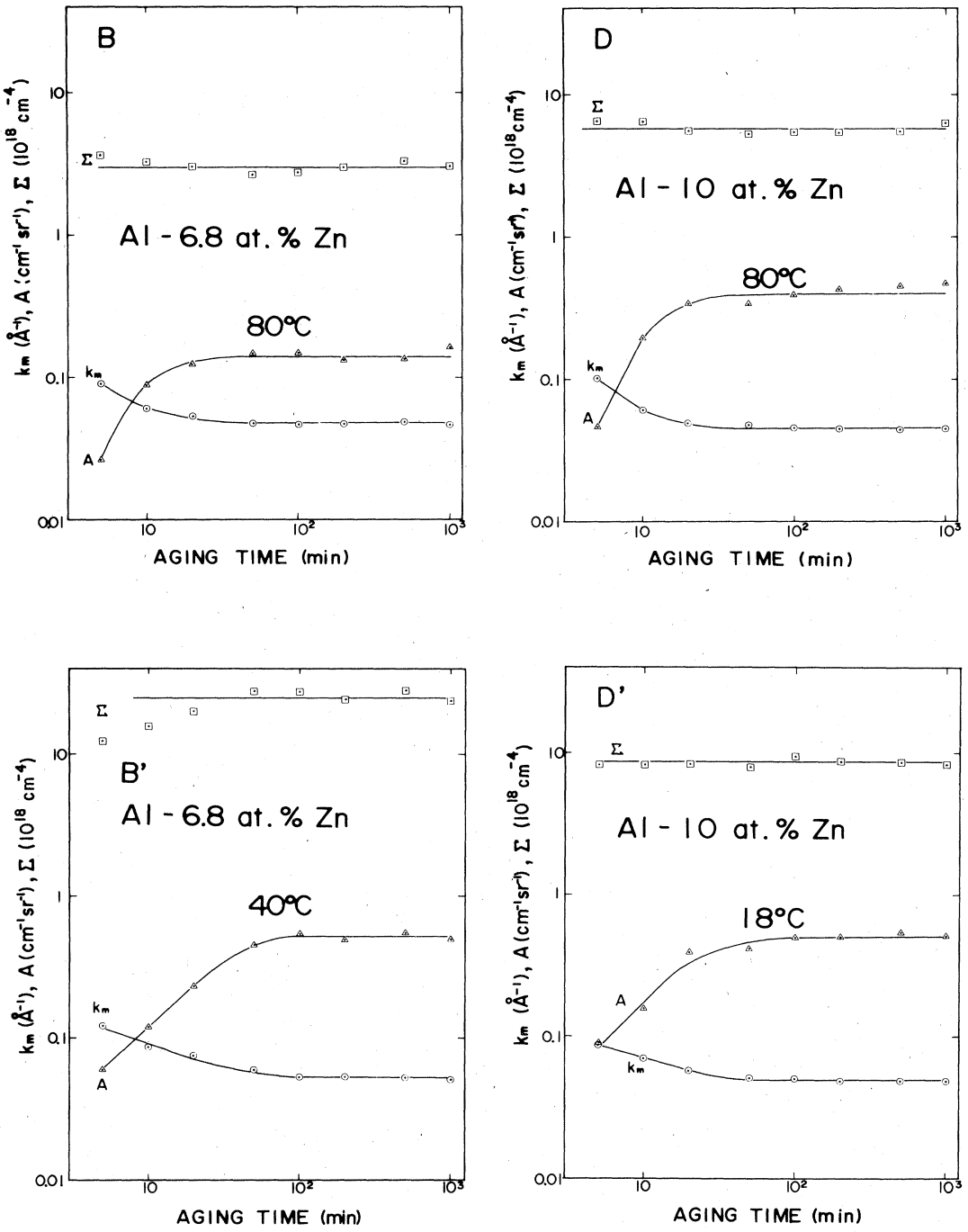

FIG. 6. (*Continued*).

From (29), (58), and (59) we obtain

$$\tilde{S}(x)=\frac{k_m^3\,\dfrac{d\Sigma(k,t)}{d\Omega}\displaystyle\int_{x_{\min}}^{x_{\max}}x^2\tilde{S}(x)dx}{\displaystyle\sum_{k=k_{\min}}^{k_{\max}}k^2\frac{d\Sigma(k,t)}{d\Omega}\Delta k}\equiv F(x,t)\ , \tag{60}$$

where α cancels out. The function $F(x,t)$ defined by (60) is different from that used by Marro, Lebowitz, and Kalos,[11] Chou and Goldburg,[12] and Hennion, Ronzaud, and Guyot[13] by the factor $\int_{x_{\min}}^{x_{\max}}x^2\tilde{S}(x)dx$, which eliminates the effect of the finite limits of the sum in the denominator and ensures the normalization $\tilde{S}(1)=1$.

Therefore, we have calculated the function $F(x,t)$ of (60) where $x=kk_m^{-1}(t)$ and compared it with Furukawa's universal scaling function $\tilde{S}(x)$ of (31) for each sample. The results are plotted in Fig. 8, in which the functions $F(x,t)$ appear to be independent of aging times t even for

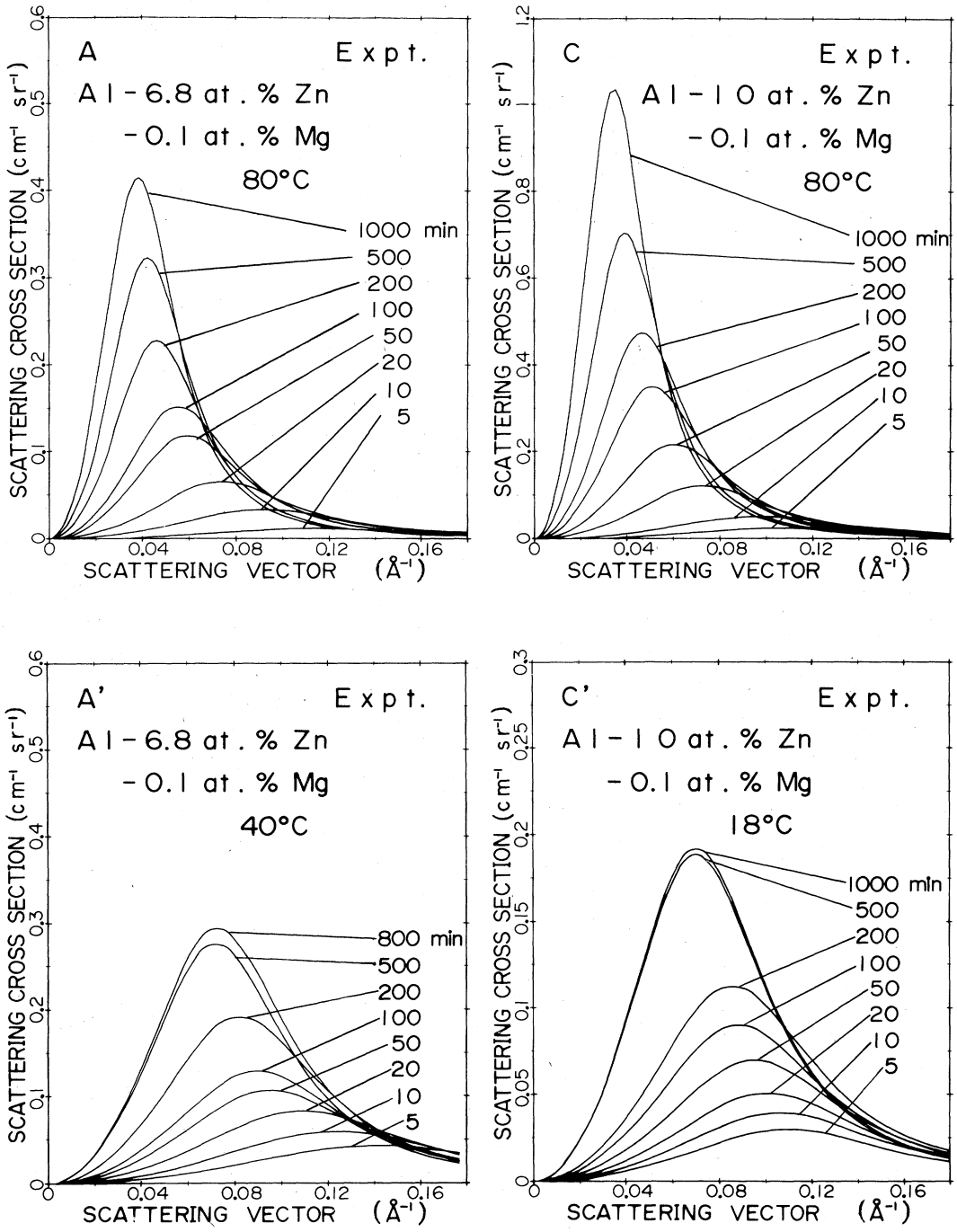

FIG. 7. Least-squares fit of the experimental data $d\Sigma(k,t)/d\Omega$ calculated from the parameters $k_m(t)$ and $A(t)$ by (53), (31), and (55) for the eight samples.

different samples and different aging temperatures, except for the sample Al—6.8 at. % Zn (B and B') in which the range of aging time of invariant $F(x,t)$ is limited to aging times less than 50 min. It is surprising to note that the calculated function $F(x,t)$ agrees excellently with Furukawa's universal scaling function $\tilde{S}(x)$ with the normalizing character $\tilde{S}(1)=1$. Since in the samples B and B' the growth of the cluster ceases at 50 min as seen in Fig. 6, some different process from the other samples might have occurred here.

D. Time evolution of the structure function

Since we were successful in correlating the universal scaled structure function $\tilde{S}(x)$ in (31) to the experimental

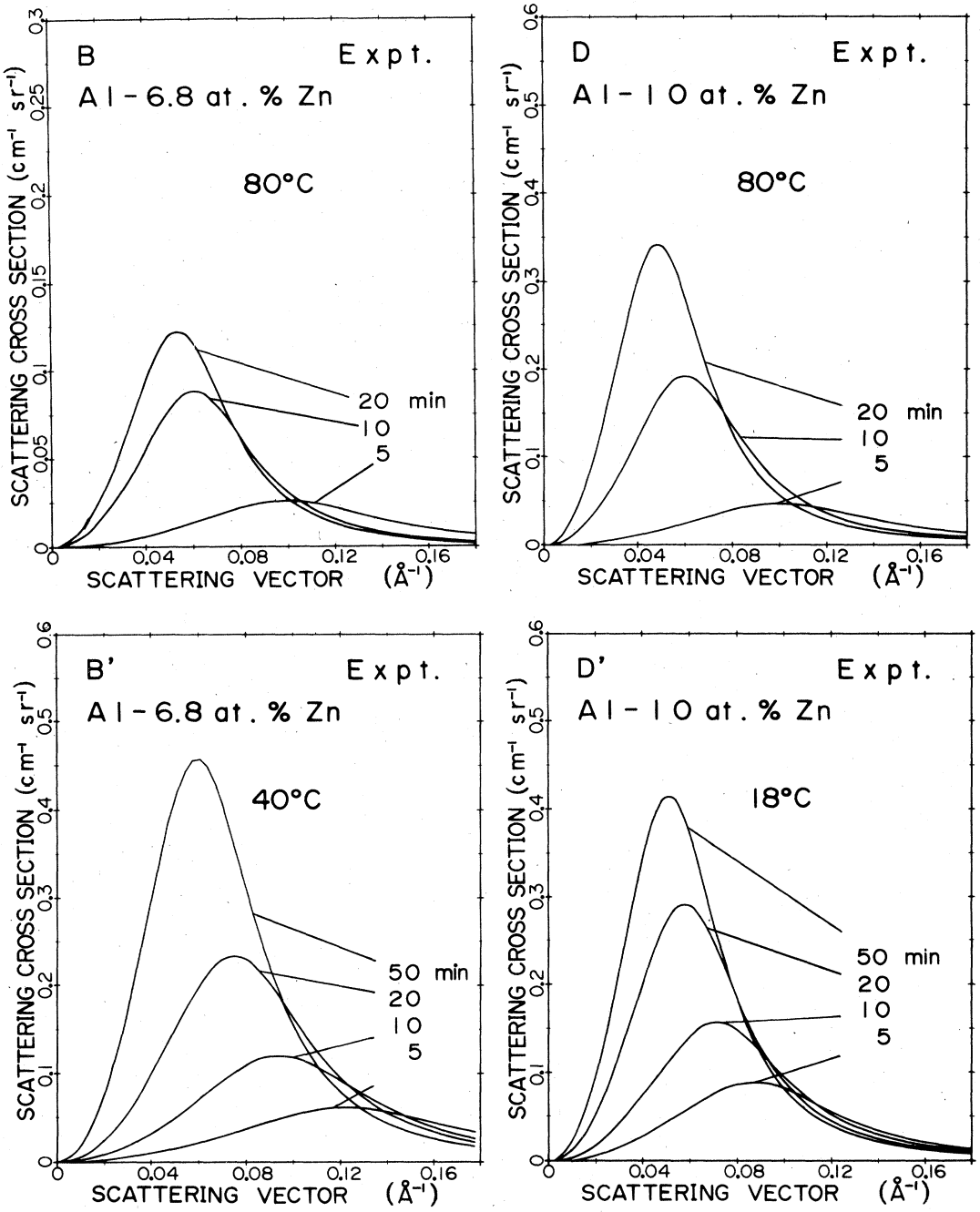

FIG. 7. (*Continued*).

TABLE IV. Parameters to calculate $\Sigma(\text{calc}) = v_a^{-2}(c-c_m)(c_p-c)(b_A-b_B)^2$ by (47). The values for c_m, c_p are those given by Gerold and Schweizer (Ref. 22).

Sample	c	c_m	c_p	$(c-c_m)(c_p-c)$	$(b_A-b_B)^2/v_a^2$
A,B	0.068	0.031	0.706	0.023 61	1.8424×10^{-12} Å^{-4}
C,D	0.100	0.031	0.706	0.041 81	1.8424×10^{-12} Å^{-4}
A',B'	0.068	0.020	0.730	0.049 64	1.8424×10^{-12} Å^{-4}
C',D'	0.100	0.015	0.745	0.054 83	1.8424×10^{-12} Å^{-4}

$v_a = 16.503$ Å^3
$b_{\text{Al}} = 0.3446\times10^{-4}$ Å
$b_{\text{Zn}} = 0.5686\times10^{-4}$ Å

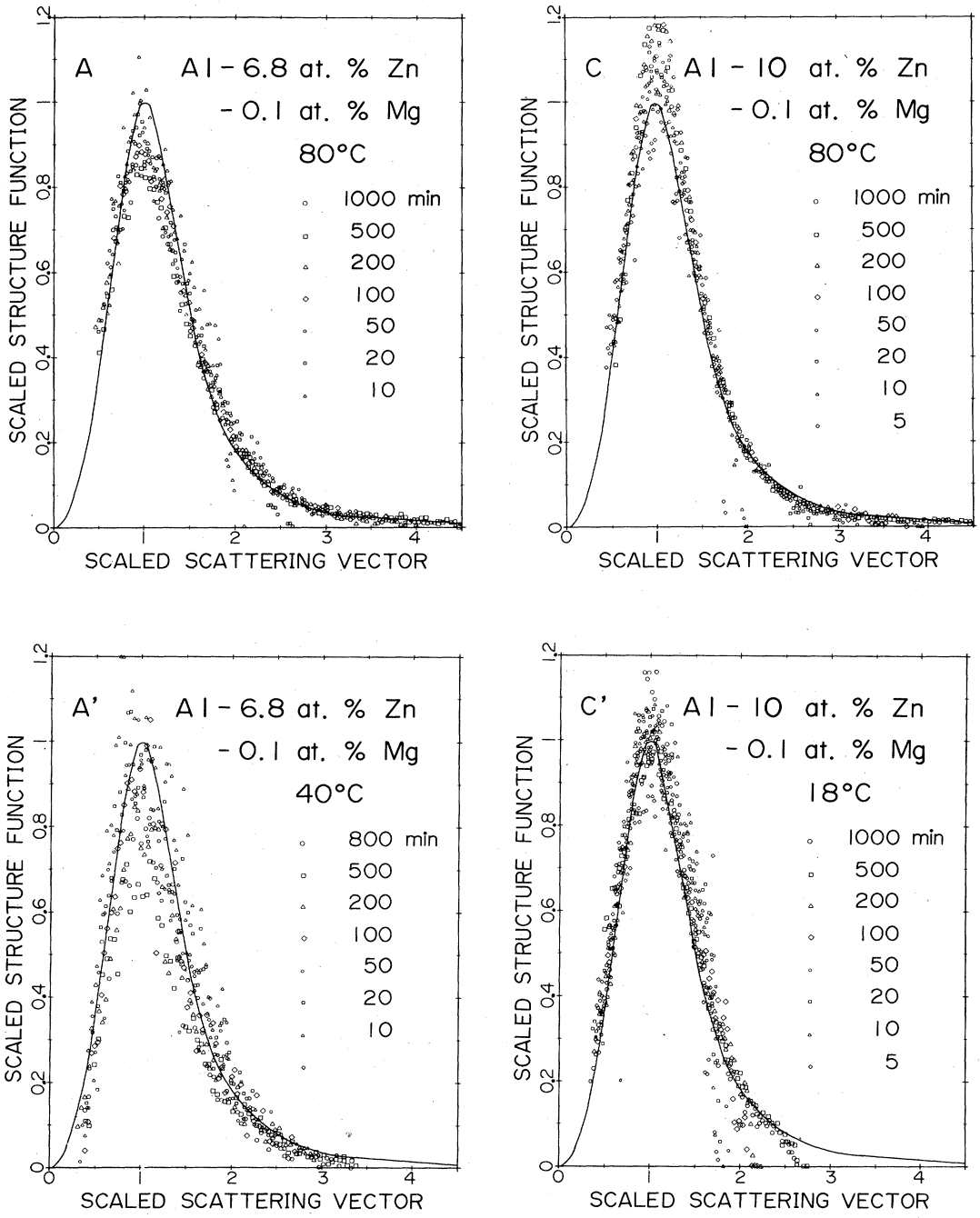

FIG. 8. Scaled structure function $F(x,t)$ defined in (60) as a function of the scaled scattering vector $x=k/k_m(t)$ at different aging times t for the eight samples. Note that there is a lack of t dependence and sample dependence. Solid curves are Furukawa's scaled structure function $\tilde{S}(x)=3x^2/(2+x^6)$ of (31).

data for the cross section $d\Sigma(k,t)/d\Omega$, we then calculated the structure function $S(k,t)$ by solving the time-evolution equation (16) for $S(k,t)$. To do this we used the values of a and ζ in Table III. The value of a is related to that of ζ by the formula (19) as listed in Table III. The remaining parameters in the framework of Furukawa's theory are only $R(1)$ in (18) or $M(1)$ in (17), which are related to one another by formula (35); if $R(1)$ is doubled, then $M(1)$ must be 32 times larger for $d=3$.

Taking proper values for $R(1)=k_m^{-1}(1)$, which were determined from an extrapolation of the curves of $k_m(t)$ in Fig. 6, and corresponding values of $k_BTM(1)$ from (35) as listed in Table III, we solved the time-evolution equation (16) with (17), (18), (20), (32), (33) by the method of

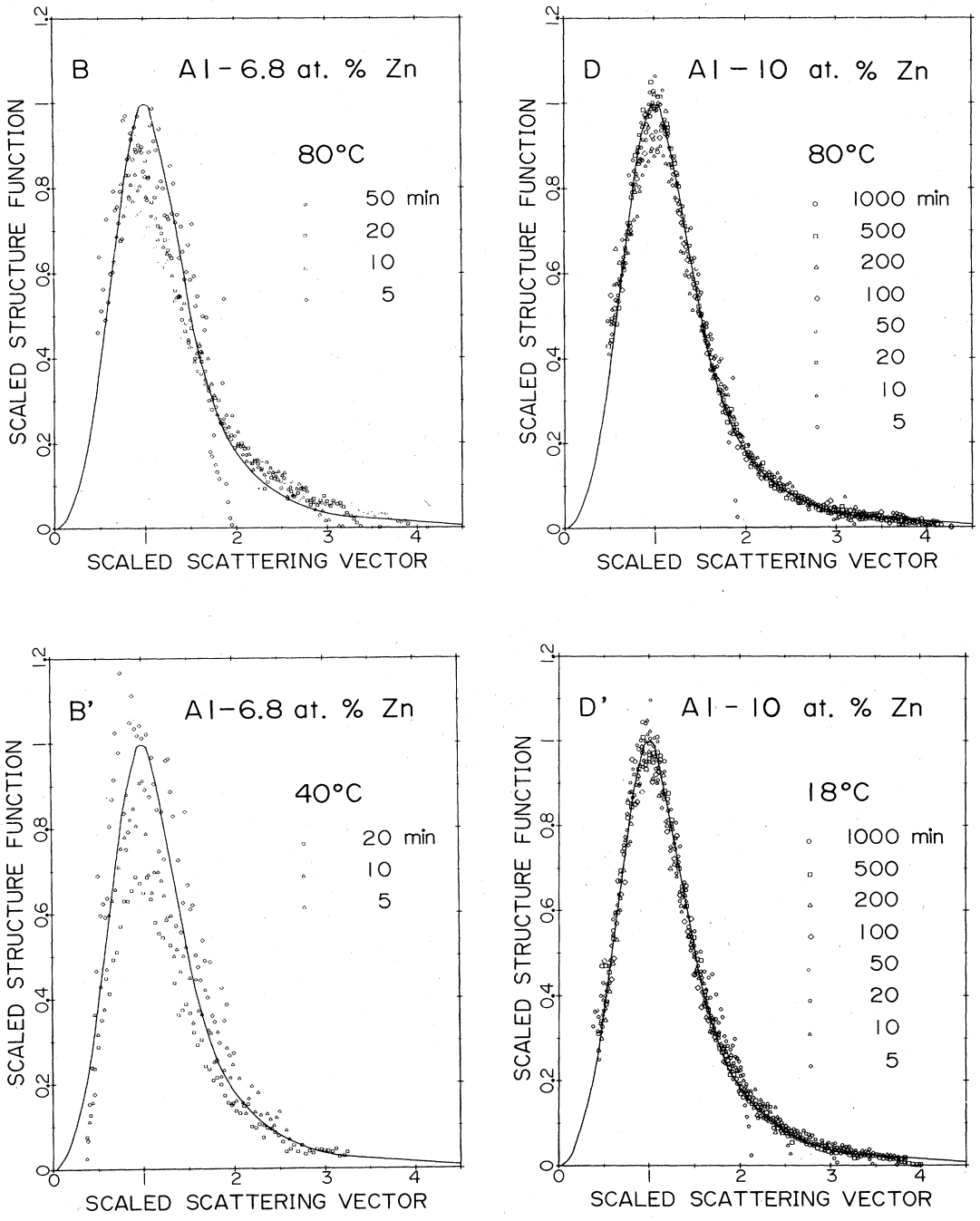

FIG. 8. (*Continued*).

Runge and Kutta to obtain $S(k,t)$ with an initial condition $S(k,1)=0$. The results of the calculation were found to be rather insensitive to the choice of the initial conditions. The neutron scattering cross sections $d\Sigma(k,t)/d\Omega$ were then calculated as in (59) by

$$\frac{d\Sigma^{\text{calc}}(k,t)}{d\Omega}=\frac{\Sigma(\text{obs})}{S(\text{calc})}S(k,t) \tag{61}$$

using the values of $S(\text{calc})$ from (29) and $\Sigma(\text{obs})$ from (58) as listed in Table I.

The results of the calculations are shown as $d\Sigma^{\text{calc}}(k,t)/d\Omega$ versus k curves in Fig. 9 for all the samples and as $d\Sigma^{\text{calc}}(k,t)/d\Omega$ versus t curves for the samples A, A', C, and C' in Fig. 10. In most cases the calculated curves were good representations of the experimental ones in Figs. 7 and 4. From the calculation some typical values for $S(k,t)$, $\chi^{-1}(k,t)$, and $D_T(k,t)$ are picked out as listed in Table V, where these values are given in units of Å^3, 10^{-7} Å^{-3}, and $\text{Å}^2/\text{min}$ $(=1.667\times10^{-18}$ $\text{cm}^2/\text{s})$,

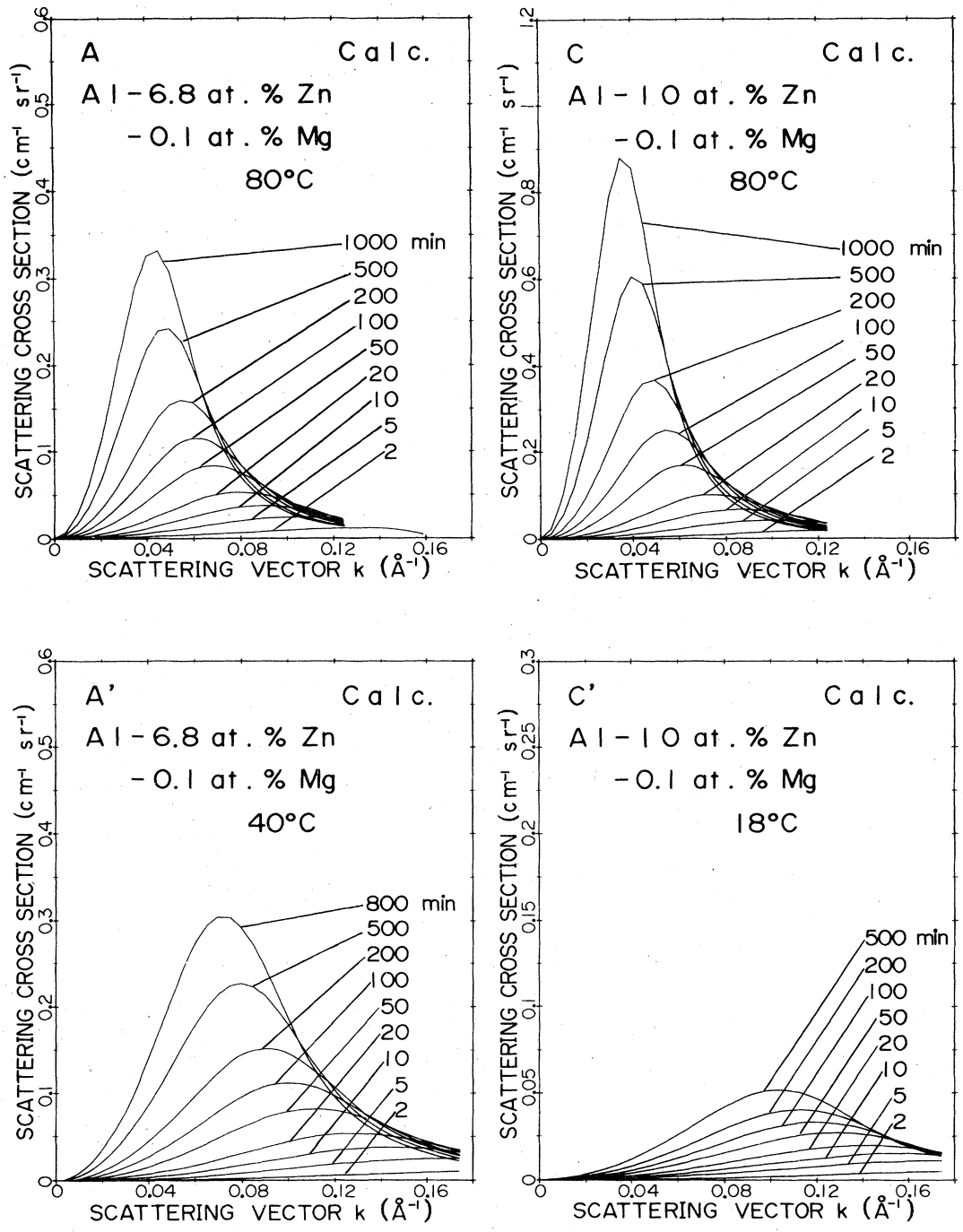

FIG. 9. Calculated value of $d\Sigma^{\text{calc}}(k,t)/d\Omega$ ($\text{cm}^{-1}\,\text{sr}^{-1}$) from solving the time-evolution equation (16) with parameters a and $R(1)$ in Table III as a function of k (Å^{-1}) at different aging times t (min) for the eight samples. Note that there is a close resemblance to the experimental data given in Fig. 7.

respectively, at typical values of aging time t and scattering vector k near the maximum of $S(k)$.

The corresponding observed scattering cross sections $d\Sigma^{\text{obs}}(k,t)/d\Omega$ and calculated ones $d\Sigma^{\text{calc}}(k,t)/d\Omega$ and their ratios

$$[d\Sigma^{\text{obs}}(k,t)/d\Omega]/[d\Sigma^{\text{calc}}(k,t)/d\Omega]$$

are listed in Table VI. The ratios are mostly close to 1 and scatter in the range from 0.5 to 5. These values seem to be satisfactory because of crudeness of the calculated model for the decomposition process and the very small number of parameters involved: only a and $R(1)$ [or alternatively ζ and $M(1)$].

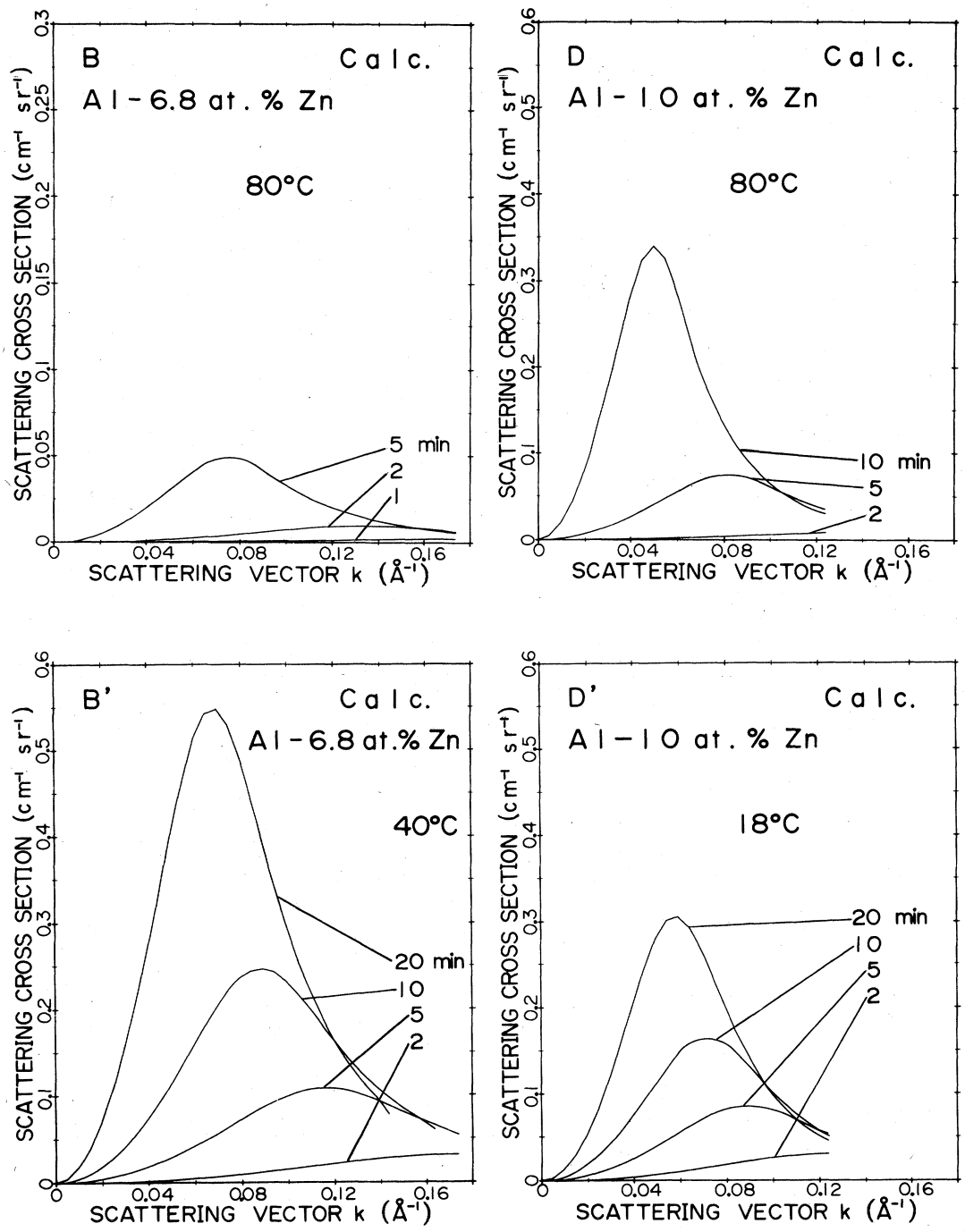

FIG. 9. (*Continued*).

E. Intercluster distance and cluster radius

The significance of the dynamic scaling law is that the cluster structure in the alloy system is characterized by only a single scaling parameter $R(t)=k_m^{-1}(t)$, which increases by a power law (18) or becomes a constant in some binary alloys at large aging times. Therefore, all the structural information must be included in the parameter $k_m(t)$. The quantities of importance in the cluster regime are (i) mean intercluster distance L between the centers of the two neighboring clusters, (ii) mean cluster radius R^*, and (iii) volume fraction f_p of the clusters surrounded by the depletion zone. Since the present results appear rather insensitive to the volume fraction of the system, we have neglected this effect hereafter. The effect of the volume fraction is planned to be discussed in a separate paper.[21]

We have calculated the Fourier transform $R(y)$ of the universal structure function $\tilde{S}(x)$ of (31) by

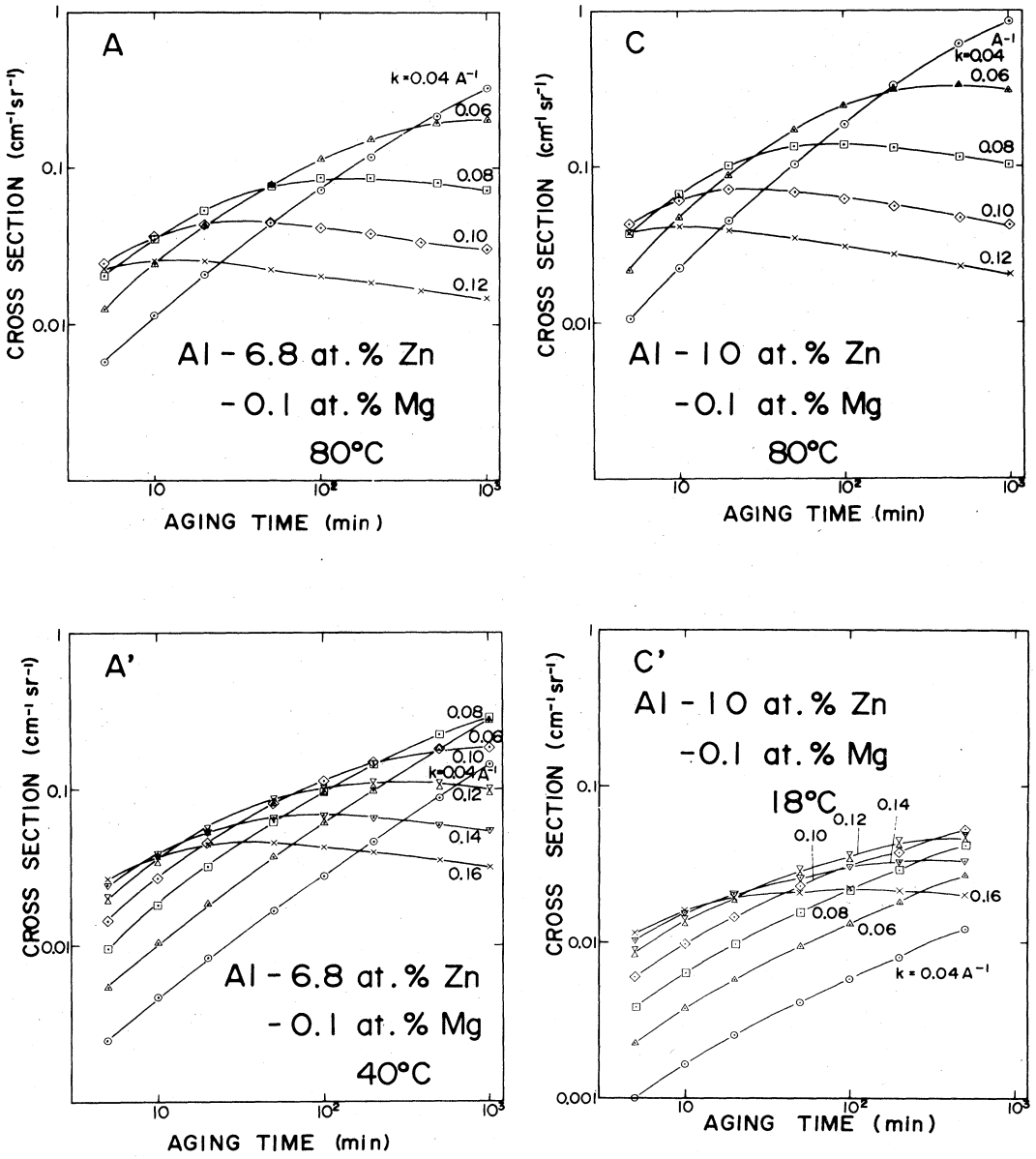

FIG. 10. Same calculated values of $d\Sigma^{\text{calc}}(k,t)/d\Omega$ ($\text{cm}^{-1}\text{sr}^{-1}$) as in Fig. 9 as a function of aging time t (min) at different scattering vectors k (Å^{-1}) for the four ternary samples A, A', C, C'. Note that there is a close resemblance to the experimental data given in Fig. 4.

$$R(y)=\frac{4\pi}{(2\pi)^3}\int_0^\infty x^2\tilde{S}(x)\frac{\sin(xy)}{xy}dx \tag{62}$$

with the transformation of the variable from $x=kk_m^{-1}$ to $y=rk_m$. The result of the numerical calculation is shown in Fig. 11. The values of y for the first zero value and the first maximum of $R(y)$ are given, respectively, by

$$y_1=2.571 \tag{63}$$

and

$$y_2=6.905\ . \tag{64}$$

Since the function $R(y)$ is a Patterson function, which represents a space-correlation function like $G(r,t)$ in (8), these values y_1 and y_2 are related to R^* and L by

$$2R^*=r_1=y_1k_m^{-1} \tag{65}$$

and

$$L=r_2=y_2k_m^{-1}\ , \tag{66}$$

where r_1 and r_2 are real distances corresponding to y_1 and y_2. Since $y_2/y_1=2.69$ is a constant, the present

TABLE V. Estimation of characteristic size $R(t)$, mobility $M(t)$, structure factor $S(k,t)$, susceptibility $\chi(k,t)$, and diffusivity $D_T(k,t)$ for typical values of aging time t and scattering vector k for each sample.

Sample	Aging time t (min)	Scattering vector k (Å^{-1})	Characteristic size $R(t)$ (Å)	Mobility $k_BTM(t)$ (Å^5/min)	Structure factor $S(k,t)$ (Å^3)	Susceptibility $\chi^{-1}(k,t)$ (10^{-7} Å^{-3})	Diffusivity $D_T(k,t)$ (Å^2/min)
A	10	0.095	13.08	21 528	2 460	2 841	6.12
	100	0.055	18.47	12 106	7 384	526	0.68
	1000	0.04	26.10	6 808	21 567	217	0.15
B	5	0.10	11.24	79 293	734	13 243	105.01
C	10	0.105	13.05	25 528	2 003	4 563	11.65
	100	0.05	19.75	20 277	8 554	505	1.02
	1000	0.035	29.89	16 107	30 862	174	0.28
D	10	0.06	16.40	320 342	2 606	3 492	111.86
A'	10	0.12	8.37	2 151	590	5 445	1.17
	100	0.09	11.55	1 078	1 851	2 302	0.25
	500	0.07	15.94	540	5 153	1 079	0.06
B'	10	0.09	10.43	17 586	986	6 157	10.83
C'	10	0.11	9.25	2 030	679	2 399	0.49
	100	0.09	11.12	510	1 555	1 312	0.07
	500	0.07	12.65	194	2 044	597	0.01
D'	10	0.07	13.73	53 087	2 442	2 224	11.80

treatment approximates $L/R^*=5.37$ to a universal constant.

From the relations (65) and (66) we have calculated the mean intercluster distance

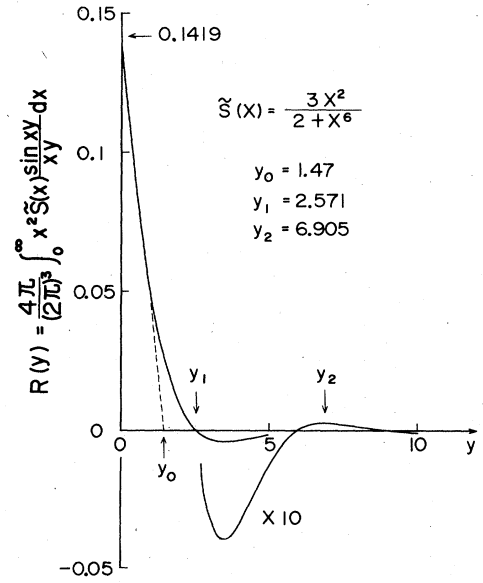

FIG. 11. Fourier transform $R(y)$ of (62) of the Furukawa's universal scaling function $\tilde{S}(x)$ of (31). y_1 and y_2 are values of y for the first zero and the first maximum of $R(y)$, respectively. y_0 is the value of y for the extrapolation of the linear portion of $R(y)$ to zero at small y.

$$L=6.905k_m^{-1} \tag{67}$$

and mean cluster radius

$$R^*=1.285k_m^{-1} \tag{68}$$

for each scattering curve for all the samples. These values are listed in Table VII, which gives a view of the real cluster structure. This method of analysis demonstrates the usefulness of the dynamic scaling law in the present system. It should be stressed that such analysis is only valid for the range of the decomposition process, where dynamic scaling holds. The conditions for the dynamic scaling to hold are that the order parameter (or the number of A and B atoms) is conserved and that the phase boundary of the cluster is well defined. The latter condition applies to the late stage of the process of the cluster growth.

The extrapolation of the linear portion of $R(y)$ to zero at small y gives

$$y_0=1.47 \tag{69}$$

as shown in Fig. 11. Since $\frac{3}{4}$ of $y_0k_m^{-1}$ gives the Porod's radius[23]

$$R_P^*=\langle R^3\rangle/\langle R^2\rangle=1.103k_m^{-1}, \tag{70}$$

where R is a radius of a cluster, the cluster radius R^* obtained from (68) in the present paper is 17% larger than the Porod's radius R_P^*.

TABLE VI. Comparison of the observed and calculated cross sections $d\Sigma(k,t)/d\Omega$ for typical values of aging time t and scattering vector k for each sample.

Sample	Aging time t (min)	Scattering vector k (Å^{-1})	$\frac{d\Sigma^{obs}(k,t)}{d\Omega}$ (cm^{-1}sr^{-1})	$\frac{d\Sigma^{calc}(k,t)}{d\Omega}$ (cm^{-1}sr^{-1})	Ratio $\frac{\left[\frac{d\Sigma^{obs}(k,t)}{d\Omega}\right]}{\left[\frac{d\Sigma^{calc}(k,t)}{d\Omega}\right]}$
A	10	0.095	0.03	0.03	1.0
	100	0.055	0.15	0.11	1.36
	1000	0.04	0.42	0.325	1.29
B	5	0.10	0.025	0.03	0.83
C	10	0.105	0.05	0.06	0.83
	100	0.050	0.35	0.25	1.4
	1000	0.035	1.03	0.88	1.17
D	10	0.06	0.19	0.28	0.68
A'	10	0.12	0.052	0.03	1.7
	100	0.09	0.130	0.11	1.18
	500	0.07	0.275	0.22	1.25
B'	10	0.09	0.12	0.25	0.48
C'	10	0.11	0.04	0.01	4.0
	100	0.09	0.09	0.025	3.6
	500	0.07	0.19	0.035	5.4
D'	10	0.07	0.16	0.16	1.0

TABLE VII. Intercluster distance $L(t)=6.905k_m^{-1}(t)$ by (67) and cluster radius $R^*(t)=1.285k_m^{-1}(t)$ by (68) at each aging time for all the samples.

Sample	L (Å) R^* (Å)	Aging time t (min) 5	10	20	50	100	200	500	1000 (*800)
A	L	61.4	75.0	93.1	115.2	123.0	147.5	161.6	178.1
	R^*	11.4	14.0	17.3	21.4	22.9	27.4	30.1	33.2
B	L	69.4	113.8	128.6	147.2	148.1	146.9	142.3	149.5
	R^*	12.9	21.2	23.9	27.4	27.6	27.3	26.5	27.8
C	L	63.2	70.5	95.1	113.4	134.1	147.7	175.2	199.7
	R^*	11.8	13.1	17.7	21.1	25.0	27.5	32.6	37.2
D	L	69.0	113.7	140.9	144.0	151.2	154.0	155.3	153.4
	R^*	12.8	21.2	26.2	26.8	28.1	28.7	28.9	28.6
A'	L	48.8	55.6	63.0	72.0	76.2	83.3	95.3	*94.2
	R^*	9.1	10.4	11.7	13.4	14.2	15.5	17.7	*17.5
B'	L	56.6	73.6	91.9	116.3	129.5	130.0	131.4	137.0
	R^*	10.5	13.7	17.1	21.7	24.1	24.2	24.5	25.5
C'	L	62.7	64.8	67.9	71.9	77.3	79.7	97.1	97.1
	R^*	11.7	12.0	12.6	13.4	14.4	14.8	18.1	18.1
D'	L	79.4	96.5	118.5	133.8	136.6	141.4	142.8	142.7
	R^*	14.8	18.0	22.1	24.9	25.4	26.3	26.6	26.6

VI. CONCLUSION

The scattering cross section $d\Sigma^{\rm obs}(k,t)/d\Omega$ of Al-Zn and Al-Zn-Mg alloys has been analyzed in terms of Furukawa's theory of the structure function $S(k,t)$. The results show that a simple dynamical scaling law $S(k,t) \propto R(t)^3 \tilde{S}(kR(t))$ holds for a wide range of aging times t for various samples with different aging temperatures. The universal structure function $\tilde{S}(x) \propto x^2/(\gamma/2+x^{2+\gamma})$ fits the experimental data excellently.

Satisfactory calculation of $d\Sigma^{\rm calc}(k,t)/d\Omega$ could be obtained by taking only two parameters and solving the time-evolution equation of $S(k,t)$ in (16). These parameters are the exponent a and the initial value $R(1)$ in the power law of the cluster size $R(t)=R(1)t^a$ in (18), or alternatively the exponent ζ and the initial value $M(1)$ in the power law of the mobility $M(t)=M_0R(t)^{-\zeta}=M(1)t^{-a\zeta}$ in (17); the values of a and ζ are related by (19) and those of $R(1)$ and $M(1)$ by (35). The overall ratio of the observed to the calculated $d\Sigma(k,t)/d\Omega$ is close to 1 and is in the range 0.5—5. Therefore, the theory represents a satisfactory model of the decomposition process in alloy systems. The derived values of diffusivity of the clusters $D_T(k,t)$ from (36), with an order of magnitude 10^{-18} cm^2/s, give some insight into the decomposition process.

ACKNOWLEDGMENT

This work has been performed at the Research Reactor Institute, Kyoto University, and the authors are very much indebted to Professor S. Okamoto and Dr. T. Akiyoshi at Kyoto University. The authors wish to thank Dr. H. Furukawa for stimulating discussions.

[1] *Nucleation,* edited by A. C. Zettlemoyer (Dekker, New York, 1969); *Nucleation II,* edited by Zettlemoyer (Dekker, New York, 1976).
[2] J. W. Cahn and J. E. Hilliard, J. Chem. Phys. **28**, 258 (1958); **31**, 688 (1959); J. W. Cahn, Acta Metall. **9**, 795 (1961); **10**, 179 (1962); **14**, 1685 (1966).
[3] M. Hillert, Acta Metall. **9**, 525 (1961).
[4] H. E. Cook, Acta Metall. **18**, 297 (1970).
[5] K. Binder and D. Stauffer, Adv. Phys. **25**, 343 (1976).
[6] J. S. Langer, M. Bar-on, and H. D. Miller, Phys. Rev. A **11**, 1417 (1975).
[7] I. M. Lifshitz and V. V. Slyozov, J. Phys. Chem. Solids **19**, 35 (1961).
[8] E. D. Siggia, Phys. Rev. A **20**, 595 (1979).
[9] K. Binder and D. Stauffer, Phys. Rev. Lett. **33**, 1006 (1974).
[10] H. Furukawa, Prog. Theor. Phys. **59**, 1072 (1978); Phys. Rev. Lett. **43**, 136 (1979); Phys. Rev. A **23**, 1535 (1981).
[11] J. Marro, J. L. Lebowitz, and M. H. Kalos, Phys. Rev. Lett. **43**, 282 (1979); J. L. Lebowitz, J. Marro, and M. H. Kalos, Acta Metall. **30**, 297 (1982).
[12] Y. C. Chou and W. I. Goldburg, Phys. Rev. A **23**, 858 (1981).
[13] M. Hennion, D. Ronzaud, and P. Guyot, Acta Metall. **30**, 599 (1982).
[14] P. A. Rikvold and J. D. Gunton, Phys. Rev. Lett. **49**, 286 (1982).
[15] H. Furukawa, Physica (Utrecht) **123A**, 497 (1984).
[16] See O. Glatter and O. Kratky, *Small Angle X-ray Scattering* (Academic, London, 1982), p. 30.
[17] The authors are indebted to Dr. H. Furukawa for this derivation.
[18] S. Komura, T. Takeda, H. Fujii, K. Osamura, Y. Toyoshima, K. Mochiki, and K. Hasegawa, Jpn. J. Appl. Phys. **22**, 351 (1983); S. Komura, T. Takeda, H. Fujii, K. Osamura, K. Mochiki, and K. Hasegawa, Physica (Utrecht) **120B**, 122 (1983).
[19] S. Komura, K. Osamura, H. Fujii, T. Takeda, and Y. Murakami, Colloid Polym. Sci. **259**, 670 (1981).
[20] S. Komura, K. Osamura, H. Fujii, and T. Takeda, Phys. Rev. B **30**, 2944 (1984).
[21] H. Furukawa (unpublished).
[22] V. Gerold and W. Schweizer, Z. Metallkd. **52**, 76 (1961).
[23] K. Osamura and K. Okuda, J. Jpn. Inst. Met. **47**, 462 (1983) (in Japanese).